

AD-A193 777

**SIMULATION OF THE RESPONSE OF A GALLIUM ARSENIDE JFET
TO SINGLE PARTICLE. (U) SCIENTIFIC RESEARCH ASSOCIATES
INC GLASTONBURY CT J P KERSKOVSKY ET AL. 30 SEP 87**

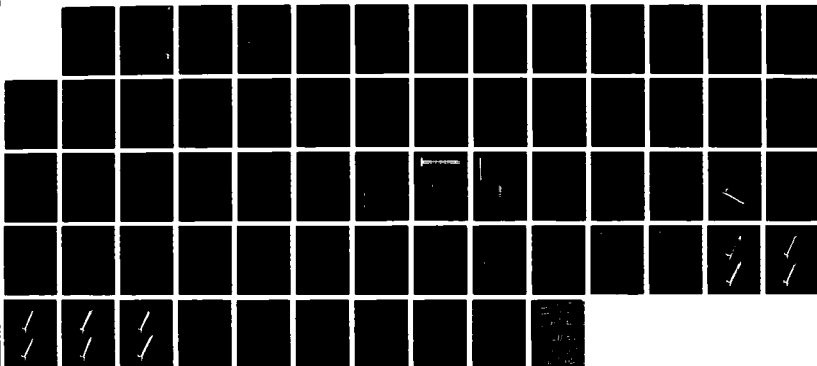
141

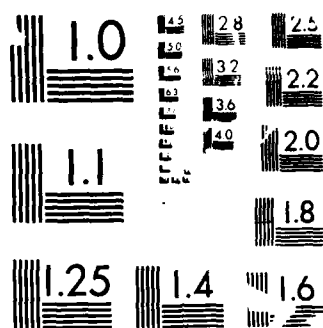
UNCLASSIFIED

BB7-920034-F N00014-87-C-2173

F/G 20/12

NL





MICROCOPY RESOLUTION TEST CHART
NBS 1963-A

DTIC FILE COPY

AD-A195 777

1 2

SIMULATION OF THE RESPONSE OF A GALLIUM ARSENIDE JFET
TO SINGLE PARTICLE RADIATION IN TWO AND THREE DIMENSIONS

REPORT: R87-920034-F

J.P. KERSKOVSKY

H.L. GRUBIN

and

B.J. MORRISON

SEPTEMBER 1987

PREPARED FOR THE NAVAL RESEARCH LABORATORY
Under Contract Number N00014-87-C-2173
by

SCIENTIFIC RESEARCH ASSOCIATES, INC.

P.O. BOX 1058

GLASTONBURY, CT 06033

DTIC
ELECTE
JUL 01 1988
S E D

Competitively awarded
Contract value \$95,684.00

This document has been approved
for public release and its use
in education is unlimited.

Unclassified

SECURITY CLASSIFICATION OF THIS PAGE

REPORT DOCUMENTATION PAGE

Form Approved
OMB No. 0704-0188

1a. REPORT SECURITY CLASSIFICATION Unclassified			1b. RESTRICTIVE MARKINGS	
2a. SECURITY CLASSIFICATION AUTHORITY N/A since Unclassified			3. DISTRIBUTION / AVAILABILITY OF REPORT	
2b. DECLASSIFICATION / DOWNGRADING SCHEDULE N/A since Unclassified				
4. PERFORMING ORGANIZATION REPORT NUMBER(S) R87-920034-F			5. MONITORING ORGANIZATION REPORT NUMBER(S)	
6a. NAME OF PERFORMING ORGANIZATION Scientific Research Associates		6b. OFFICE SYMBOL (If applicable)	7a. NAME OF MONITORING ORGANIZATION Naval Research Laboratory	
6c. ADDRESS (City, State, and ZIP Code) P.O. Box 1058 Glastonbury, CT 06033-1058			7b. ADDRESS (City, State, and ZIP Code) Washington, DC 20375-5000	
8a. NAME OF FUNDING / SPONSORING ORGANIZATION		8b. OFFICE SYMBOL (If applicable)	9. PROCUREMENT INSTRUMENT IDENTIFICATION NUMBER N00014-87-C-2173	
8c. ADDRESS (City, State, and ZIP Code)			10. SOURCE OF FUNDING NUMBERS	
			PROGRAM ELEMENT NO.	PROJECT NO.
			TASK NO.	WORK UNIT ACCESSION NO.
11. TITLE (Include Security Classification) Simulation of the Response of a Gallium Arsenide JFET to Single Particle Radiation in Two and Three Dimensions				
12. PERSONAL AUTHOR(S) Kreskovsky, J.P., Grubin, H.L., Morrison, B.J.				
13a. TYPE OF REPORT Technical		13b. TIME COVERED FROM 870801 TO 870930		14. DATE OF REPORT (Year, Month, Day) 870930
15. PAGE COUNT				
16. SUPPLEMENTARY NOTATION				
17. COSATI CODES			18. SUBJECT TERMS (Continue on reverse if necessary and identify by block number)	
FIELD	GROUP	SUB-GROUP	Transient Three-Dimensional Simulation	
			Two-Dimensional Single Particle GaAs JFET	
19. ABSTRACT (Continue on reverse if necessary and identify by block number)				
<p>The response of a GaAs JFET to single particle radiation is simulated in two and three dimensions through numerical solution of the drift and diffusion, and Poisson's equations. Scaling of the particle track density is introduced in the two-dimensional simulation. The two- and three-dimensional results are compared. Qualitative agreement between the three-dimensional simulation are observed, but quantitative differences in current pulses and charge collected at the devices contacts are present.</p>				
20. DISTRIBUTION / AVAILABILITY OF ABSTRACT <input type="checkbox"/> UNCLASSIFIED/UNLIMITED <input checked="" type="checkbox"/> SAME AS RPT. <input type="checkbox"/> DTIC USERS			21. ABSTRACT SECURITY CLASSIFICATION Unclassified	
22a. NAME OF RESPONSIBLE INDIVIDUAL			22b. TELEPHONE (Include Area Code)	22c. OFFICE SYMBOL

CONVERSION TABLE

MULTIPLY —————> BY —————> TO GET

TO GET <————— BY <————— DIVIDE

angstrom	1.0×10^{10}	meter
electron volt	1.602×10^{-1}	joule
foot	3.018×10^{-1}	meter
inch	2.54×10^{-2}	meter
micron	1.0×10^{-6}	meter

Accession For	
NTIS GRA&I	<input checked="" type="checkbox"/>
DTIC TAB	<input type="checkbox"/>
Unannounced	<input type="checkbox"/>
Justification	<i>per</i>
By _____	
Distribution/	
Availability Codes	
Dist	Avail and/or Special
<i>A-1</i>	



TABLE OF CONTENTS

SECTION	PAGE
CONVERSION TABLE	
LIST OF ILLUSTRATIONS	v
1. INTRODUCTION	1
2. ANALYSIS	3
2.1 Governing Equations	3
2.2 Mobility and Diffusivity Models	5
2.3 Boundary Conditions and Doping Specification	6
2.4 Modeling of the Track	7
3. THE NUMERICAL METHOD	9
3.1 Philosophy of the Solution Procedure	9
3.2 Implementation on a Vector Machine	13
4. RESULTS	15
4.1 Device Structure Considered	15
4.2 Details of the Particle Track	15
4.3 The Computational Procedure	15
4.4 The Equilibrium Solution	16
4.5 Comparison of the Two- and Three-Dimensional Transient Results	16
5. SUMMARY AND CONCLUSIONS	21

LIST OF ILLUSTRATIONS

- Figure 1. Schematic representation of the JFET device considered showing the location of the particle strike.
- Figure 2. Grid in X-Z plane, a, and blow up of grid in the channel region, b.
- Figure 3. Grids in the X-Y and Y-Z planes as in the three-dimensional simulation.
- Figure 4. Steady state contours of a) $\log N$, b) $\log P$ and c) potential in the JFET.
- Figure 5. Steady state contours of electron density in the channel region of the JFET, a) contours of N , b) contours of $\log N$.
- Figure 6. Steady state contours of hole density in the channel region of the JFET, a) contours of P , b) contours of $\log P$.
- Figure 7. Steady state contours (a) and surface plot (b) of the potential in the JFET.
- Figure 8. Current pulses as a function of time at source, drain and gate contacts after particle strike, 2-D result.
- Figure 9. Current pulses as a function of time at source, drain and gate contacts after particle strike, 3-D result.
- Figure 10. Percent of total particle generated charge collected at gate contact for 2-D simulation.
- Figure 11. Percent of total particle generated charge collected at gate contact for 3-D simulation.
- Figure 12. Comparison of potential distribution along the track axis for the 2-D and 3-D simulations with the steady state result and the 3-D result 12.5 μm below the track axis 40 psec following the particle strike.
- Figure 13. Net electron and hole charge collected at all contacts, 2-D result.
- Figure 14. Net electron and hole charge collected at all contacts, 3-D result.
- Figure 15. Contours of $\log N$ at a) 10 psec, b) 40 psec, c) 100 psec, d) 200 psec, and e) 400 psec following the particle strike for the 2-D case.
- Figure 16. Contours of $\log N$ at a) 10 psec, b) 40 psec, c) 100 psec, d) 200 psec, and e) 400 psec following the particle strike for the 3-D case in the X-Z plane of the particle track.
- Figure 17. Contours of $\log P$ at a) 10 psec, b) 40 psec, c) 100 psec, d) 200 psec, and e) 400 psec following the particle strike for the 2-D case.

LIST OF ILLUSTRATIONS (continued)

- Figure 18. Contours of $\log p$ at a) 10 psec, b) 40 psec, c) 100 psec, d) 200 psec, and e) 400 psec following the particle strike for the 3-D case in the X-Z plane of the particle track.
- Figure 19. Contours of equa-potential at a) 10 psec, b) 40 psec, c) 100 psec, d) 200 psec and e) 400 psec following the particle strike for the 2-D case.
- Figure 20. Contours of equa-potential at a) 10 psec, b) 40 psec, c) 100 psec, d) 200 psec and e) 400 psec following the particle strike for the 3-D case in the X-Z plane of the particle track.
- Figure 21. Comparison of 2-D and 3-D result for potential surface in the X-Z plane of the particle track 10 psec following the strike.
- Figure 22. Same as Figure 21 except at $T = 40$ psec.
- Figure 23. Same as Figure 21 except at $T = 100$ psec.
- Figure 24. Same as Figure 21 except at $T = 200$ psec.
- Figure 25. Same as Figure 21 except at $T = 400$ psec.
- Figure 26. Potential contours in two Y-Z planes.
Left, $0.5\mu\text{m}$ from the contact surface, in the channel
and right, $8.24\mu\text{m}$ from the contact surface,
in the substrate, at $t = 10$ psec.
- Figure 27. Potential contours in the Y-Z planes.
Left, $0.5\mu\text{m}$ from the contact surface, in the channel
and right, $8.24\mu\text{m}$ from the contact surface,
in the substrate, at $t = 40$ psec.
- Figure 28. Potential contours in the Y-Z planes.
Left, $0.5\mu\text{m}$ from the contact surface, in the channel
and right, $8.24\mu\text{m}$ from the contact surface,
in the substrate, at $t = 100$ psec.
- Figure 29. Potential contours in the Y-Z planes.
Left, $0.5\mu\text{m}$ from the contact surface, in the channel
and right, $8.24\mu\text{m}$ from the contact surface,
in the substrate, at $t = 200$ psec.
- Figure 30. Potential contours in the Y-Z planes.
Left, $0.5\mu\text{m}$ from the contact surface, in the channel
and right, $8.24\mu\text{m}$ from the contact surface,
in the substrate, at $t = 400$ psec.

SECTION 1

INTRODUCTION

In an effort to aid in the design and fabrication of devices more resistant to single event upsets and to gain understanding of the internal dynamics of devices struck by single radiation particles, device researchers have turned to numerical simulation. Early studies of such phenomena involved two-dimensional simulations of the response of two-terminal N⁺P diode structures to single particle radiation [1,2,3]. These studies gave light to a result coined the field-funneling effect.

However, the picture which emerged from the initial diode simulations was incomplete. As was demonstrated in [4,5] the response of more complex devices was significantly different from that of simple diodes. For example, in 2-D simulations of JFETS and MESFETS [4] it was found that the spreading of excess charge deposited in the device substrate lowered the substrate resistance substantially and provided a source-drain current path in a device that was initially in the off state. Additionally, only a small portion of the charge deposited by the radiation particle was collected at a struck gate node. Similarly, simulations of CMOS and bipolar or multi-layered devices [4,5] showed the existence of extremely complex current paths, aside from those at the struck node, and including such phenomena as plasma wires or ion shunts across the base region of bipolar devices. Such effects have, as a result, been included in circuit simulations [6].

Even with the additional information provided by 2-D device simulation, modeling of SEUs using circuit simulations is limited. There is substantial interaction between the external circuit and the device. Thus, it is important to couple the device simulation to the external circuit. Such an approach has been followed in [7] where a two-dimensional simulation of a CMOS memory cell, coupled to the external circuit, was performed.

While the present authors agree strongly that drift and diffusion simulations of the devices in question must be coupled to the external circuitry, the approach taken in [7] still has a major shortcoming; the drift and diffusion simulations were limited to two dimensions. While it is true that much has been learned through two-dimensional simulations about device response characteristics when subjected to single particle radiation, the physics involved is inherently three-dimensional. In [8,9] the present authors demonstrated the significant inaccuracies resulting from the assumption of two-dimensionality by carefully comparing results from both two- and three-dimensional simulations of charge collection in a simple silicon diode. It was also demonstrated that the two-dimensional results for the collection time and the current pulse could be made to follow the three-dimensional result by properly scaling the track density. Such a scaling result was recently found to apply to an NMOS structure which was simulated in both two and three dimensions in [10]. However, even in these cases it was cautioned that the transport process in two dimensions was highly inaccurate. Thus, while two-dimensional simulations may provide a useful tool, results thus

obtained must be, at least, verified through selective three-dimensional computations.

While the need to perform three-dimensional transient simulations is readily apparent, a major drawback has been the computational intensity of such simulations. In 1981, Buturla, et. al. [11] reported on a three-dimensional transient simulation involving the reverse recovery of an ellipsoidal junction. The computational segment of the device simulated was $1.25 \times 1.25 \times 2.5 \mu\text{m}$ and a finite element grid of 600 nodes with 810 elements was used. Thirty time steps were taken and the simulation required approximately 5 hours of CPU time [11] on an IBM 370/168 computer. By 1985, the situation had improved. The three-dimensional transient simulation of charge collection performed by the present authors [8,9] only required approximately 3.5 hours of CPU time on a Cray 1 computer using a finite difference procedure with 17,500 grid points and 350 time steps. The algorithm used in those simulations, while highly efficient, did not take advantage of the Cray's vector architecture. However, the algorithm was ideally suited for vectorization and it was estimated that when vectorized, run times would be reduced by at least an order of magnitude making practical three-dimensional transient simulations a reality for more complex structures.

This was indeed found to be a conservative estimate in [10] where a vectorized version of this algorithm was applied to the simulation of a silicon NMOS device. The simulation of the NMOS structure utilized a three-dimensional mesh of 21560 points. 1050 time steps were taken during the simulation which required only 1.44 hours of CPU time on a Cray 1 computer. This was roughly 16 times faster than the run time projected using a scalar version of the same solution algorithm.

The present report continues to address the need for three-dimensional simulations of single particle effects and two-dimensional scaling approaches through the application of this vector algorithm to the simulation of a GaAs JFET structure.

SECTION 2

ANALYSIS

2.1 GOVERNING EQUATIONS.

The discussion which follows is general in that allowance is made for heterojunctions. However, in the JFET structure considered, no heterojunctions are present. The governing continuity equations thus take the form

$$\frac{\partial N}{\partial t} = \frac{1}{e} \nabla \cdot J_n + G - R \quad (1)$$

$$\frac{\partial P}{\partial t} = -\frac{1}{e} \nabla \cdot J_p + G - R \quad (2)$$

where the current densities are given by

$$J_n = e \left[N \mu_n \nabla(\psi + F_n) + D_n \nabla N \right] \quad (3)$$

$$J_p = -e \left[P \mu_p \nabla(\psi + F_p) + D_p \nabla P \right] \quad (4)$$

The quantities F_n and F_p are introduced to account for variations in the conduction and valence band energy levels, and are related to the electron affinity, the density of states and the energy band gap as [12]

$$F_n = \frac{1}{e} (\chi + kT \ln N_c) \quad (5)$$

$$F_p = \frac{1}{e} (\chi + E_g - kT \ln N_v) \quad (6)$$

The gradients of F_n and F_p give rise to local "effective fields" at material interfaces which may augment or retard drift transport across the interface. G and R in Eqs. (1) and (2) are generation and recombination terms. The recombination term is given as

$$R = \frac{NP - N_i^2}{\tau_p(N + N_i) + \tau_n(P + N_i)} + r(N + P)(NP - N_i^2) \quad (7)$$

Here τ_n and τ_p are recombination lifetimes whereas r is a recombination

rate constant. The first and second terms in Eq. (7) represent Shockley-Read-Hall and Auger recombination, respectively. For GaAs, the carrier lifetimes are on the order of 1 nsec.

Generation of carriers results from two effects in the present simulations; impact ionization, and generation due to the energy absorbed from the incident radiation particle. The authors have shown [8] that at bias levels of a few volts impact ionization in a simple diode would not contribute to excess carrier generation. Since the bias levels imposed here on reversed junctions are, at a maximum, on the order of one volt, reverse breakdown of such junctions is not anticipated and impact ionization should not effect the results. However, this process is modeled in the present simulations following the standard approach for completeness. Generation due to impact ionization is expressed as

$$G_i = \frac{1}{e} (\alpha_n |J'_n| + \alpha_p |J'_p|) \quad (8)$$

where α_k , ($k = n, p$) is given by

$$\alpha_k = A_k \exp \left[- \left(\frac{b_k}{|E|} \right)^{m_k} \right] \quad (9)$$

The values of the constants A , b and m for GaAs are given in Table 1. It is noted that the current densities used in Eq. (8) are limited to the drift component of the particle currents only, following Sze [13], rather than the full particle current (drift plus diffusion). The present authors believe that this approach is more realistic because, for example, in a reversed bias diode ideally the current flow is zero with drift and diffusion currents balancing exactly. As a result, breakdown of the diode at high reverse bias would not be predicted. When only the drift component is considered, avalanche generation will occur at high fields and reverse breakdown will occur.

Generation due to thermalization by the incident particle is modeled in a straight forward manner as

$$G_r = \frac{N_\alpha(r)}{\tau_\alpha} \exp [-t(r)/\tau_\alpha] \quad (10)$$

Here $N_\alpha(r)$ is the concentration of particles generated within the track, and can be a function of distance along the track. τ_α represents a time constant thermalization, typically taken as 3 psec, and $t(r)$ represents the time elapsed from when the radiation particle penetrates the device to a specific point along its track. For example, a 5MeV alpha particle possesses a range of 18.5 μm in GaAs and travels at an average velocity of approximately 1.56×10^9 cm/sec. Thus, on average, carrier generation will begin at the entry point of the particle track 1.18psec before generation at the end of the track.

While the model is sufficiently general to include the above-mentioned effects, in the present simulations N_A was assumed constant along the entire track length, and the delay time along the track was neglected. Therefore, generation was assumed to take place simultaneously and uniformly along the entire track length.

Since space charge effects must be considered in the present analysis, a self-consistent electric field must be determined from Poisson's equation

$$\nabla \cdot \epsilon \nabla \psi = -\rho = e(N-P-C) \quad (11)$$

where C is the net doping distribution of donor and acceptor ions. Here we note that, due to the heterojunction formulation, the permittivity could be spatially dependent.

2.2 MOBILITY AND DIFFUSIVITY MODELS.

The mobility model used in the present simulations allows for negative differential mobility of GaAs electrons. The electron velocity is given by

$$V_n = [\mu_0 E + a(E/E_v)^2 + b(E/E_v)^3 + c(E/E_v)^4] \frac{1}{1 + (E/E_v)^4} \quad (12)$$

where the low field mobility, μ_0 , exhibits density dependence follow the data of Blakemore [14]. An empirical fit to this data yields

$$\mu_0 = 5200 - 2800 \tanh \left[0.902992 [(\log N) - 16.845] \right] \quad (13)$$

The mobility is obtained by dividing the velocity, V_n by the electric field, E . For holes,

$$\mu_p = \frac{\mu_0}{\left[1 + \left(\frac{\mu_0 |E|}{V_{sat}} \right)^\beta \right]^{1/\beta}} \quad (14)$$

where $|E|$ is the magnitude of the electric field and V_{sat} is the saturated drift velocity.

The diffusivity is then determined using the Einstein relation

$$D = \frac{kT}{e} \mu \quad (15)$$

where k is Boltzmann's constant, and T is the temperature (taken here as constant, 300°K). The constants used in the mobility expression are given in Table 2.

2.3 BOUNDARY CONDITIONS AND DOPING SPECIFICATION.

The specification of the doping distribution and the boundary conditions determine the type of device under consideration and the bias point. For the two- and three-dimensional comparative simulations considered here, the device structure is taken as two-dimensional in the X-Z plane. Three-dimensional effects are introduced by the presence of the ionizing particle track. Thus, a direct evaluation of the limitation of a two-dimensional modeling approach can be made. The doping distribution for the device is thus given as

$$C(x,z) = N_D - N_A \quad (16)$$

Boundary conditions are required for ohmic contacts and free surfaces. The carrier densities at ohmic contacts are determined through the assumption of zero space charge

$$N - P = C \quad (17)$$

together with the assumption of thermal equilibrium

$$NP = N_i^2 \quad (18)$$

The concentrations of electrons and holes at ohmic contacts, as well as the initial distribution of carriers throughout the device, are determined by simultaneous solution of Eqs. (17 and 18).

The potential at ohmic contacts is specified relative to the vacuum level, as it must be if a consistent treatment of heterojunctions is to be retained.

At N-type contacts

$$\Psi = V_{APP} + \frac{kT}{e} \ln \frac{N}{N_C} - \frac{\chi}{e} \quad (19)$$

and at P-type contacts

$$\Psi = V_{APP} - \frac{kT}{e} \ln \frac{P}{N_V} - \frac{E_g}{e} - \frac{\chi}{e} \quad (20)$$

It should be noted that in the absence of any variation in the electron affinity, and under the assumption that the Fermi level is centered between

the conduction and valence bands (i.e. $N_C = N_V$), Eq. (19), for example, reduces to the commonly used relationship for homojunctions,

$$\Psi = V_{APP} + \frac{kT}{e} \ln \frac{N}{N_i} \quad (21)$$

where the contributions to the built-in potential from the band gap and electron affinity are ignored since they are equal at all contacts.

At free surfaces, the normal component of electric field and current density are set to zero.

2.4 MODELING OF THE TRACK.

Obviously, modeling of the track in three dimensions poses no significant problems. The generation of the associated excess carriers, on a per-unit volume basis, has been discussed previously. Thus, all that need be specified in three dimensions is the total number of carriers to be generated, the range of the ionizing particle (or track length) and an assumption of the initial diameter of the track. The only approximation required, when using a three-dimensional Cartesian coordinate system, is that the initial cross-section of the track be modeled by a series of square cells. Thus, the initial track cross-section will only approximate a circular cross-section. The accuracy of this initial approximation will depend on the size of the grid spacing relative to the track diameter. However, even when the grid spacing is on the order of the track radius, this initial approximation rapidly decays to a cylindrical distribution, as demonstrated in three-dimensional simulations of a simple diode [8,9].

In two dimensions, however, significant approximations must be made. As discussed in [8], in two dimensions only the X-Z plane of the device is considered, and the excess particle generated carriers are introduced over an area of this plane. The length of this region is taken as the particle penetration or track length while the width is taken as the initial track diameter. Both the device and the track extend indefinitely in the unmodeled third dimension. The particle track is thus represented by a slab of excess charge rather than as a cylinder. To yield meaningful results from the simulations, a depth in the third dimension must be specified. When choosing this arbitrary depth several constraints provide guidance. However, not all of the constraints can be met simultaneously. The constraints considered are as follows:

- (1) the total ion-generated excess charge,
- (2) the density of carriers in the track,
- (3) the volume of the slab representing the particle track, and
- (4) the physical depth of the device.

Since the device structure is itself assumed to be two-dimensional, the fourth constraint also sets the device contact areas.

It is obviously necessary to introduce the correct number of electron-hole pairs for a given particle, thus the first constraint must be met. The remaining three constraints are all interdependent. If the depth of the device is chosen as the actual physical device depth, then the contact areas will be correct but the volume of the slab representing the particle track will be much greater than the actual cylindrical track, and to maintain the proper total charge the track density must be reduced below its actual level. On the other hand, if the device depth is chosen to be on the order of the initial track diameter, then the volume of the slab of excess carriers will closely approximate the actual track volume and the carrier density within the track will be near the actual value. However, the device contacts will be much smaller than in reality. In a recent, comparative two- and three-dimensional study performed by the present authors [8], it was found that the first approach, choosing the device depth as the relevant parameter and adjusting the track density, yielded similar current pulses for both two- and three-dimensional simulations; the second choice resulted in significantly larger collection times and over-predicted field distortions. The first approach was also found to yield excellent results in the NMOS simulation reported in [10]. Thus, the approach followed in the two-dimensional device simulation performed here is to assign a value to the depth parameter representative of the device depth.

It should be cautioned, however, that while the results of the comparative studies of [8] and [10] gave good predictions of the current pulse, compared to the full three-dimensional simulation, the details of carrier transport in the devices were significantly different. Therefore, in complex devices, such as that considered here, if carrier transport details are important the present approach may be only qualitative at best. For this reason, the authors continue to advocate that full three-dimensional simulations be performed for complex structures, at least to verify the two-dimensional modeling approach. This comparison and verification is one of the objectives of the present research applied to a GaAs JFET.

SECTION 3

THE NUMERICAL METHOD

3.1 PHILOSOPHY OF THE SOLUTION PROCEDURE

A detailed discussion of the solution technique, including the development of consistent difference approximations to the governing equations, is given in [15]. Thus, the discussion here will be limited to the philosophy behind the technique and implementation on a vector machine.

In an effort to develop a highly efficient solution technique to the system of Eqs. (1, 2 and 11) it is first recognized that this system is a coupled, non-linear system. If solved as a coupled system, it will require utilization of methods designed for coupled elliptic equations to obtain a solution at each time step. These methods typically introduce some outer iteration to treat nonlinearity and the methods used to solve the difference approximations to the linearized system are often computationally intensive in two dimensions, and totally impractical to implement in three. By contrast, the method used here eliminates nonlinear iteration, uses a noniterative yet highly efficient procedure to solve the difference approximations to the continuity equations, and uses an extremely efficient iterative technique to solve the equation governing the potential. As shall be discussed, these solution techniques are also ideally suited for implementation on vector machines and/or parallel processors making them even more attractive.

The first step in this procedure is to decouple Poisson's equation from the continuity equation in a manner which does not adversely affect stability of the overall solution algorithm. This is accomplished by reformulating the continuity equations by expanding the drift term, and substituting the space charge for the Laplacian of the potential. After manipulation, the result is

$$\begin{aligned} \frac{\partial N}{\partial t} = & -\nabla \cdot N\mu_n \nabla F_n - \nabla \mu_n N \cdot \nabla \psi - \mu_n \frac{Ne}{\epsilon} (N-P-C) \\ & + \mu_n \frac{N}{\epsilon} \nabla \epsilon \cdot \nabla \psi + \nabla \cdot D_n \nabla N + G - R \end{aligned} \quad (22)$$

$$\begin{aligned} \frac{\partial P}{\partial t} = & \nabla \cdot P\mu_p \nabla F_p + \nabla \mu_p P \cdot \nabla \psi + \mu_p \frac{Pe}{\epsilon} (N-P-C) \\ & - \mu_p \frac{P}{\epsilon} \nabla \epsilon \cdot \nabla \psi + \nabla \cdot D_p \nabla P + G - R \end{aligned} \quad (23)$$

To ensure conservation of total current, Poisson's equation is recast as a

statement of total current,

$$\begin{aligned} \frac{\partial \nabla \cdot \epsilon \nabla \psi}{\partial t} = & -e \nabla \cdot N \mu_n \nabla (\psi + F_n) - e \nabla \cdot P \mu_p \nabla (\psi + F_p) \\ & + e \nabla \cdot (D_n \nabla N - D_p \nabla P) \end{aligned} \quad (24)$$

From Eqs. (22-24) it is easily shown that at steady state, Poisson's equation is satisfied exactly. A small error is introduced in transients, as discussed in [15].

Eqs. (22-24) form the basis of the solution algorithm. To advance the solution from t^n to $t^{n+1} = t^n + \Delta t$, the mobilities and diffusivities are evaluated using the electric field and carrier densities at t^n . Additionally, the gradients of potential appearing in the second and fourth terms on the R.H.S. of Eqs. (22 and 23) are evaluated at the t^n level. This effectively decouples the continuity equations from the total current constraint and allows the carrier concentrations to be advanced first. This decoupling does not introduce a stability constraint [15].

The advance in time of the carrier concentrations is performed by solving the continuity equations (Eqs. (22 and 23)) as a block 2x2 coupled system through application of a linearized block implicit (LBI) method [16]. The continuity equations are of the form

$$\frac{\partial \phi}{\partial t} = D(\phi) + S(\phi) \quad (25)$$

where $\phi = (N, P)^T$, $D(\phi)$ represent those terms in Eqs. (22 and 23) which contain spatial derivatives of ϕ , and $S(\phi)$ represent source terms such as the recombination, generation and space charge terms. Eq. (25) is then time differenced using a backwards differencing scheme,

$$\frac{\Delta \phi^{n+1}}{\Delta t} = D(\phi)^{n+1} + S(\phi)^{n+1} + O(\Delta t) \quad (26)$$

where $\Delta \phi^{n+1} = \phi^{n+1} - \phi^n$, and the superscripts refer to the time level. $D(\phi)^{n+1}$ and $S(\phi)^{n+1}$ are then formally linearized in time using a Taylor series expansion about the solution at time t^n as

$$G(\phi)^{n+1} = G(\phi)^n + \Delta t \left. \frac{\partial G(\phi)}{\partial \phi} \right|_n \frac{\partial \phi}{\partial t} \Big|_n + O(\Delta t^2) \quad (27)$$

Substituting a forward difference approximation for the time derivative in Eq. (26)

$$G(\phi)^{n+1} = G(\phi)^n + \left. \frac{\partial G(\phi)}{\partial \phi} \right|_n \Delta \phi^{n+1} + O(\Delta t^2) \quad (28)$$

Eq. (26) may then be expressed as

$$(A + \Delta t L) \Delta \phi^{n+1} = \Delta t [D(\phi)^n + S(\phi)^n] + O(\Delta t) \quad (29)$$

where

$$A = I - \Delta t \left. \frac{\partial S(\phi)}{\partial \phi} \right|_n \quad (30)$$

and

$$L = - \left. \frac{\partial D(\phi)}{\partial \phi} \right|_n \quad (31)$$

When the L operator is approximated by three-point difference approximations Eq. (29) represents a block 2x2 matrix equation which may be written at each grid point in the solution domain. In one dimension, the result is a block 2x2 tridiagonal coefficient matrix which may be solved efficiently using direct block tridiagonal elimination. For two- or three-dimensional approximations, while the block size remains 2x2, since it is determined by the number of coupled equations, the bandwidth of the resulting coefficient matrix increases significantly. In two dimensions, on a square mesh of NxN points, the rank of the coefficient matrix is of order N² and the bandwidth is of order N. In three dimensions, with an NxNxN mesh, the rank of the coefficient matrix is of order N³ and the bandwidth of order N². Obviously, use of direct inversion techniques for such matrices, for even relatively small meshes, would result in a computationally intensive and inefficient solution procedure. For this reason, iterative matrix solvers are often used. However, for large meshes even these iterative solvers may become prohibitive and should be avoided, if possible. This can be accomplished, due to the parabolic nature of continuity equations, by applying a consistently split ADI procedure [17] to solve Eq. (29). To split or factor Eq. (29), the L operator is separated into its directional components, $L = L_x + L_y + L_z$, and Eq. (29) is rewritten as a sequence of one-dimensional systems along each mesh line in the x, y and z directions respectively:

$$(A + \Delta t L_x) \Delta \phi^* = \Delta t [D(\phi)^n + S(\phi)^n] \quad (32a)$$

$$(A + \Delta t L_y) \Delta \phi^{**} = A \Delta \phi^* \quad (32b)$$

$$(A + \Delta t L_z) \Delta \phi^{***} = A \Delta \phi^{**} \quad (32c)$$

Elimination of the intermediate steps in Eq. (32) yields

$$(A + \Delta t L_x) A^{-1} (A + \Delta t L_y) A^{-1} (A + \Delta t L_z) \Delta \phi^{***} = \Delta t [D(\phi)^n + S(\phi)^n] \quad (33)$$

Comparison of Eqs. (29 and 33) shows that Eq. (33) approximates Eq. (29) to $O(\Delta t^2)$, thus

$$\Delta\phi^{n+1} = \Delta\phi^{***} + O(\Delta t^2) \quad (34)$$

While this factorization error may place additional restrictions on the time step when considering accuracy, the overall reduction in computational effort will typically more than offset this limitation. Each of Eqs. (32) is tridiagonal, thus direct elimination can be implemented in a highly efficient manner. On an $N \times N \times N$ mesh, the factorization reduces the need to solve a rank N^3 matrix to a task requiring the solution of $3N^2$ tridiagonal matrices of rank N . Since only tridiagonal matrices need to be solved, regardless of the mesh structure, the number of operations per mesh point remains constant and the computational effort required to solve the continuity equations varies linearly with total mesh points when implemented on a scalar machine.

Having advanced the carrier concentrations, the total current constraint, Eq. (24) must be solved for the potential. Since the carrier densities at t^{n+1} are now known, Eq. (24) can be differenced fully implicitly while only ψ remains unknown. It must be noted that while a time derivative appears in Eq. (24), this equation remains elliptic and must be solved iteratively. To accomplish this Eq. (24) is recast as

$$\rho \Delta\psi = \frac{\partial \nabla \cdot \epsilon \nabla \psi}{\partial t} + e \nabla \cdot N \mu_n \nabla(\psi + F_n) + e \nabla \cdot P \mu_p \nabla(\psi + F_p) - e \nabla \cdot (D_n \nabla N - D_p \nabla P) \quad (35)$$

and Eq. (35) expressed as

$$(A + \frac{1}{\rho} L) \Delta\psi^{i+1} = \frac{1}{\rho} [D(\psi)^i + S(\psi)^i] \quad (36)$$

where

$$A = I - \frac{1}{\rho} \left. \frac{\partial S(\psi)}{\partial \psi} \right|^i \quad (37)$$

and

$$L = - \left. \frac{\partial D(\psi)}{\partial \psi} \right|^i \quad (38)$$

Here, $D(\psi)$ includes the first three terms on the R.H.S. of Eq. (35) and $S(\psi)$ the last term. The superscript "i" refers to an iteration index and ρ is an acceleration parameter which varies both spatially and from iteration to iteration. Eq. (36) may be ADI split, as were the continuity equations, following Eqs. (32). However, in contrast to the continuity equations, the total current constraint must be iterated to convergence at each physical time step. With the proper choice of acceleration parameters

this can be accomplished rapidly and efficiently. It should also be noted that since the D operator is linear in ψ , $L = -D$ and the D operator need only be computed at the start of the iteration and stored. Similarly, the S operator is not a function of ψ in this case, thus $\partial S/\partial \psi = 0$. The S operator also need be computed only once and stored. At convergence, $\Delta\psi^{i+1} = \Delta\psi^{***}$ will go to zero and, as may be observed from Eq. (33), the factorization error will also go to zero and the difference approximations to Eq.(24) is solved exactly. This completes the advance of the solution from t^n to t^{n+1} . The process is then repeated for the next time step.

3.2 IMPLEMENTATION ON A VECTOR MACHINE.

The procedure described in the previous section has proven to be a very efficient procedure. The basic efficiency of the algorithm lies in the low operations count of the procedures used to solve the systems of difference equations. On a three-dimensional mesh with a total of N_T grid points, the number of operations required to solve Eqs. (29 and 36) is given as [15]

$$OPT_{3D} \approx 108N_T + (15N_T)I \quad (39)$$

where I is the number of iterations required in the solution of the total current constraint. On a two-dimensional mesh this reduces to

$$OPT_{2D} \approx 72N_T + (10N_T)I \quad (40)$$

since only two of the ADI sweeps need to be performed. For a one-dimensional problem the result is

$$OPT_{1D} \approx 36N_T + (5N_T)I \quad (41)$$

Note that in each case, the multi-dimensional operation count is simply the one-dimensional result times the number of dimensions.

In three dimensions, the total number of grid points N_T is the product of the number of mesh points in each direction, respectively

$$N_T = N_x * N_y * N_z \quad (42)$$

Thus, the three-dimensional operation count is the sum of the operations required for each of Eqs. (32a - 32c)

$$\begin{aligned} OPT_{3D} &\approx (36N_x + 5N_x I) * N_y N_z \\ &+ (36N_y + 5N_y I) * N_x N_z \\ &+ (36N_z + 5N_z I) * N_x N_y \end{aligned} \quad (43)$$

where there are $N_y N_z$ "x" implicit lines, $N_x N_z$ "y" implicit lines and $N_x N_y$ "z" implicit lines. Since each of the "x" implicit lines requires the same sequence of operation to be performed to solve Eq. (32a), then the solution of the "x" implicit lines can be done in parallel, or in a vector loop. Similarly, the operations required to set up or generate the difference equations which constitute Eq. (32a) can also be performed in vector loops. As a result, rather than set up and then solve Eq. (32a) along each of the $N_y N_z$ "x" implicit lines one at a time, all $N_y N_z$ "x" implicit lines may be processed at once in a single vectored loop, providing sufficient storage is available. The $N_y N_z$ scalar operations are replaced by a single vector operation. In general, a vector length, VL, may be defined, and the number of vector loops needed to solve Eq. (32a) will be the integral part of $(N_y N_z)/VL$. Similar results are obtained for the "y" and "z" implicit counterparts, Eqs. (32b and c). The number of vector operations required to solve Eq. (32), for three-dimensional problems then becomes

$$OPTV_{3D} \approx 108N_T/VL + (15N_T/VL)I \quad (44)$$

If an $N_x N_y N_z$ mesh is used and sufficient storage exists for $VL = N^2 = N_T^{2/3}$, then

$$OPTV_{3D} \approx 108N_T^{1/3} + (15N_T^{1/3})I \quad (45)$$

For two-dimensional problems the result is

$$OPTV_{2D} \approx 72N_T^{1/2} + (10N_T^{1/2})I \quad (46)$$

Comparison of Eqs. (45 and 46) with their scalar counterparts, Eqs. (39 and 40), immediately reveals that there are substantial savings for both two- and three-dimensional algorithms; that the larger the problem, the greater the potential savings; and the potential savings is greater in the three-dimensional case. However, in the present simulations, the vector length was limited to $VL = N_T^{1/3}$ for the three-dimensional problems and $VL = N_T^{1/2} = N$ for two-dimensional problems. Thus, while Eq. (46) yields an indication of the performance obtained in two dimensions, the three-dimensional performance followed the estimate

$$OPTV_{3D} \approx 108N_T^{2/3} + (15N_T^{2/3})I \quad (47)$$

SECTION 4

RESULTS

4.1 DEVICE STRUCTURE CONSIDERED.

The structure of the GaAs JFET device considered under the present research is shown in Fig. 1. The device structure is taken to be invariant in the third dimension (into the page) thus the three-dimensional effects are limited to those due to the particle track. The device, which is representative of current JFET technology, consists of an N^+ source and drain, doped to $2 \times 10^{17}/\text{cm}^3$, a p-gate doped to $2 \times 10^{17}/\text{cm}^3$ and a $1.0 \times 10^{17}/\text{cm}^3$ N type channel. The substrate is π GaAs, nominally p-type ($1 \times 10^{14}/\text{cm}^3$). The dimensions of the device are shown in the figure but it is worthy to note that the source-drain spacing is $3\mu\text{m}$. The device is taken as $25\mu\text{m}$ wide (into the page). The source and drain diffusions penetrate $0.5\mu\text{m}$ into the device. The channel is $0.3\mu\text{m}$ deep and the gate diffusion penetrates $0.2\mu\text{m}$ into the channel.

The device was biased in the off state with 1 volt applied to the drain and 0 volts applied to the source and the gate contact. The substrate was also grounded.

4.2 DETAILS OF THE PARTICLE TRACK.

The incident particle considered in the present simulations is a 5MeV alpha particle. As shown in Fig. 1, the particle is assumed to enter the device through the gate diffusion and penetrate approximately $18.5\mu\text{m}$, the range of such a particle in GaAs [18]. Since 4.5eV are required to produce a single electron-hole pair in GaAs, a 5MeV particle will generate about 9.375×10^5 electron-hole pairs. In the present simulations these excess carriers are introduced uniformly along the track. Since the initial track radius is of the order of 1000\AA , this results in a track density of $1.38 \times 10^{18}/\text{cm}^3$ for the three-dimensional simulation where the track is represented by a square cross-section $.2 \times .2\mu\text{m}$. For the two-dimensional simulation the track is modeled as a slab $.2\mu\text{m}$ thick, $18.5\mu\text{m}$ long and extending the width of the device, $25\mu\text{m}$. Recall that in two dimensions the calculations are performed on a per-unit width basis and, as discussed in section 2.4, the assignment of the assumed width of the device is critical. Using the actual device width was found to yield similar results between two- and three-dimensional simulations in [8] and [10] and this approach is followed here. Using $25\mu\text{m}$ as the width parameter yields a track density of $1.103 \times 10^{16}/\text{cm}^3$ substantially below the actual track density, but yielding the correct total number of excess carriers.

4.3 THE COMPUTATIONAL PROCEDURE.

The first step in performing the simulations is the construction of a suitable finite difference grid. For the two-dimensional simulation an unequally-spaced mesh of 51 x points by 44 z points was used. The mesh in the X-Z plane

is shown in Fig. 2. The mesh is structured to give adequate resolution of junctions and the particle track. For the three-dimensional simulation, the same mesh was used in the X-Z plane with 18 grid points, unequally spaced, in the y direction. The X-Y and Y-Z mesh structures are shown in Fig. 3. Note that since the particle is assumed to strike the center of the device, the solution will be symmetric about the center, and only half the device need be modeled in three dimensions. Thus, the y grid extends from the center of the device (and particle track) to the device edge. Note the orientation of the coordinates in Figs. 1 through 3 as this will aid in the interpretation of contour plots presented later.

The next step is to compute the solution for the initial, undisturbed state. Since, in the absence of the particle track, this solution is invariant in the y direction, the solution need only be computed in two dimensions. This result was used for the initial condition in both the two-dimensional and three-dimensional transient charge collection simulations.

The two-dimensional transient simulation was then computed using 2000 time steps and a CPU time on a Cray X/MP24 computer of 14.13 minutes or 0.00018 sec/grid point/time step. This was 14 times faster than the original scalar version of the code. In the three-dimensional simulation smaller time steps were required initially to maintain sufficient accuracy with the higher initial track density. Thus, the three-dimensional simulation required 2075 time steps yielding a CPU time, on a Cray X/MP24, of 6.83 hours or about 0.00029 sec/grid point/time step. This was roughly 15 times faster than the projected run time based on the original, scalar code.

4.4 THE EQUILIBRIUM SOLUTION.

Since the equilibrium solution is not a function of the Y coordinate direction, it need be examined in only a single X-Z plane. In Fig. 4 contours of the log of electron and hole concentrations, and potential are shown. The density contours are equally spaced with an increment one order of magnitude. The potential contours are also equally spaced with an increment of 0.1 volts. The results are as expected, showing the N^+ diffusions and depletion of the electrons in the channel. Figs. 5 and 6 show details of the contours of the carrier densities in the channel region of the device in both a linear (Figs. 5a and 6a) and a log scale. The tick mark on the bottom of the figures is $2.5\mu\text{m}$ from the contact surface. Fig. 7 shows an enlargement of the potential contours in the same region and a surface plot of the steady state potential distribution. The typical high field region at the drain side of the gate is clearly evident in this figure.

The device structure is such that it is a normally off device, thus at the applied bias level, there is negligible source-drain current. This provides an excellent initial condition for the charge collection simulations to be performed. Any current observed during the transient will be a direct result of the disturbance generated by the particle strike.

4.5 COMPARISON OF THE TWO- AND THREE-DIMENSIONAL TRANSIENT RESULTS

The main point of interest in the comparison of the two- and three-dimensional

charge collection transient simulations is the shape and duration of the current pulse at the struck gate node and the charge collected there. The current pulses at other contacts are also of interest as they may affect device operation. The current pulses at the source, gate and drain contacts are shown in Fig. 8 for the two-dimensional case. The positive drain current indicates electrons leaving the device while the negative source current represents injection of electrons. The gate current is made up of electron, hole and displacement current, however, it is predominantly hole current and represents collection of holes from the particle track. The results shown in Fig. 8 are very similar, both in duration and magnitude, to the results obtained for a JFET in [4] despite the fact that the source, drain and gate diffusions were more heavily doped ($5 \times 10^{18}/\text{cm}^3$) in [4].

As shown in Fig. 8, the gate current in the two-dimensional simulation increases rapidly to a peak of 0.325ma in less than 10psec and then decays in an exponential manner. By 100psec the gate current is approximately 0.02ma and further decay takes place on a very long (relatively) time scale. By 400psec the gate current is only about 0.006ma and continues to decay slowly.

The initial peak in the gate current is associated with the collection of holes generated in the gate depletion region. Once these holes are collected the gate current decays and additional holes are collected slowly as they diffuse into the junction region. As will be discussed subsequently, field funneling at the P⁺N junction between the gate and channel does not occur, at least not in the usual sense.

The current pulses at the source and drain are also shown in Fig. 8. The drain current exhibits a rapid rise to its initial peak which occurs at approximately 10psec. This initial peak is associated with the collection of the electrons generated in the gate junction. A small positive peak is also observed at the source. This is also associated with the collection of electrons generated in the gate junction. However, this peak rapidly decays and the source current becomes negative, balancing the drain current, which is well in excess of the gate current. Obviously the source-drain current is not simply associated with the collection of the excess, particle generated carriers. Rather, it is a result of the spreading of the excess carriers generated in the substrate. As in the simulation reported in [4], the excess carriers lower the substrate resistance and open a current path around the gate allowing a source-drain current to flow. This current will continue to flow for a substantially longer time than that associated with the gate transient since the carriers in the substrate move primarily by diffusion and are collected slowly, or recombined. Since, as time goes on, the excess carrier concentrations become small, the diffusion and recombination processes will become even slower and the elimination of excess carriers from the substrate will drag on. The source-drain current will continued to flow during much of this time.

The current pulses at the source, gate and drain contacts for the three-dimensional simulation are shown in Fig. 9. Here it is observed that while the results are qualitatively similar, quantitative differences are apparent. The peak in the gate current is only 0.18ma. However, after 25psec the gate currents are almost identical. The drain current does not exhibit the rapid rise to an initial peak and the positive peak in the source current

is greater. Additionally, the source-drain current is not as high.

The charge collected at the gate contact for the two- and three-dimensional cases is shown in Figs. 10 and 11, respectively. As shown, the results reflect the differences in the initial peak in the gate current. After 400psec the two-dimensional result indicates the collection of more than 6% of the particle-generated charge, or charge contained in the first $1.1\mu\text{m}$ of the track. By comparison the three-dimensional result shows only slightly more than 5% of the charge collected, corresponding to the first $0.925\mu\text{m}$ of the track. By 400psec, however, the rate of charge collection is nearly the same for both cases.

The differences in the results for the two- and three-dimensional cases are somewhat surprising in light of the excellent agreement obtained in [8] for a silicon diode, and [10] for an NMOS device using a similar method to scale the particle track. However, the discrepancy between the present results and those of [8] and [10] can be explained by consideration of differences in the device structures and the response of the field to the particle track. In [8] and [10] the diffusions of the struck N^+ regions were deep enough so that at the contacts the electric field was very small. Since the carrier density at the contact was fixed, and since the low field mobility in the region of the contact was also constant, the contact resistance was also constant giving rise to a linear current-field relationship at the contact. Thus, in the scaled two-dimensional simulations of [8] and [10], while the field disturbance at the contact was smaller than the localized disturbance in the contact field observed in the three-dimensional results, the two-dimensional disturbance occurred over the entire device width. As discussed in [8] the result is that the average field over the contact area is the same in both cases and, since a linear current-field relationship exists, the contact currents and collected charge were equal. In the present JFET simulations the gate P^+ diffusion is only on the order of 2000\AA deep and space charge effects are present near the contact surface. As a result the field at the contact is not low. In fact it is high enough to result in velocity saturation. Therefore, a linear current-field relationship does not exist and even with an equal average field over the contact area the contact currents are not equal. The higher local field in the three-dimensional case does not give rise to a linear increase in the local current density because the velocity is in saturation. Rather, the increase in the field results in a lower diffusivity which upsets the local balance between drift and diffusion and modulates the local current density in a nonlinear fashion. In the present case this results in a lower initial gate current for the three-dimensional simulation.

The localization of the field distortions in the three-dimensional case, and the absence of the field funneling effect at the gate diffusion are illustrated in Fig. 12. Here the potential along the axis of the particle track is compared for the two- and three-dimensional cases with the steady state result. The potential along a line parallel to the track axis in an X-Z plane $12.5\mu\text{m}$ below the track, on the surface of the device, is also shown. The results are at 40psec following the particle strike. The gate contact is at a distance of zero. The potential distribution along the track axis shows reasonable agreement between the scaled two-dimensional simulation and the three-dimensional result. It is readily apparent that there is no field

funneling effect down the axis of the track, drawing holes toward the gate. Instead, the field in this region increases significantly, with the greater increase occurring in the three-dimensional case. However, the results can be interpreted as a field funneling effect which draws electrons from both the gate diffusion and the π -type substrate into the N channel. The comparison 12.5 μ m below the track axis shows that in the gate-channel junction there is very little effect of the disturbance although the disturbance is felt slightly in the substrate.

The distortion of the potential along the axis of the track and elsewhere within the device can be explained by examining the net electron and hole charge collected at all device contacts. This result for the two-dimensional simulation is shown in Fig. 13 and for the three-dimensional simulation in Fig. 14. As can be seen, during the initial phase of the transient more electrons are collected than holes. Thus, the net excess charge in the device is positive, and in accordance with Poisson's equation and Green's theorem the curvature of the potential surface must become more negative, and the field at the device contacts must change in a consistent manner. This is discussed in detail for the case of a simple two-terminal diode in [11] and the arguments brought forth there apply equally to any device. The distorted potential along the track axis is consistent with these requirements.

It should be observed in Figs. 13 and 14 that after approximately 150psec, the net charge imbalance remains constant. This imbalance is expected to remain nearly constant until all the excess electrons are collected from the device or recombined. At that time the source-drain current will decay to zero and the remaining excess holes will be collected (at the gate and substrate) and the potential will return to its original state. Based on a constant collection rate for holes obtained from the slope of the curve in Fig. 14 at 400psec, the time elapsed before complete field restoration (complete charge collection) will be at least another 17.4nsec. Since the gate current, where most of the holes are collected, continues to decrease, as shown in Figs. 8 and 9, the average collection rate will typically be at most half the value at 400psec, and the time for complete restoration may be in excess of 35nsec. This time scale may be reduced by recombination, however, as the carriers diffuse throughout the substrate the excess carrier densities become very low and the recombination effects will become unimportant.

Fig. 15 shows contours of the log of the electron concentration at five instants during the transient for the two-dimensional case. In these figures, as in Fig. 4, the contour spacing is one order of magnitude. The contacts are on the left side of the figure with the source contact at the bottom of the left side. In Figs. 15a, b and c the contour value in the center of the track is $2 \times 10^{15}/\text{cm}^3$. In Figs. 15d and e, only the $2 \times 10^{14}/\text{cm}^3$ contour remains. Similar results are shown in Fig. 16 for the X-Z plane containing the particle track in the three-dimensional simulation. Again, the contour spacing is one order of magnitude, however, the maximum contour values at the center of the track are larger. In Fig. 16a the center contour is at $2 \times 10^{17}/\text{cm}^3$. The center contour value in Figs. 16b, c and d is $2 \times 10^{16}/\text{cm}^3$ and in Fig. 16d the value is $2 \times 10^{15}/\text{cm}^3$. Thus, while the spreading of the excess charge appears qualitatively similar in the two- and three-dimensional simulations quantitatively they are quite different. This

is a direct result of the higher initial track density of the three-dimensional simulation and shows the stronger, more localized disturbance present in three dimensions. Also note the difference in the contours in the immediate region of the gate diffusion.

Similar contours for hole concentrations are shown in Figs. 17 and 18. In Fig. 17, for the two-dimensional results, the maximum contour value associated with the track is $2 \times 10^{15}/\text{cm}^3$ in 17a through d and $2 \times 10^{14}/\text{cm}^3$ in 17e. In Fig. 18 the maximum contour values are $2 \times 10^{17}/\text{cm}^3$ for 18a, $2 \times 10^{16}/\text{cm}^3$ for 18b, c and d, and $2 \times 10^{15}/\text{cm}^3$ for 18e.

Potential contours for the two- and three-dimensional simulations, in the X-Z plane of the particle track are shown in Figs. 19 and 20 at the same instants in time as the electron and hole contours. In these figures the increment between potential contours is 0.1 volts. There is good quantitative and qualitative agreement between these comparisons indicating that the scaling of the particle track density still holds even though the limited gate current alters the current and charge collection transient somewhat. The slightly greater initial disturbance of the potential along the track axis is clearly evident in Fig. 20. A more vivid comparison of the potential disturbance in this plane is shown in Figs. 21 through 25 where the 2-D and 3-D potential surfaces are compared side-by-side. The similarity in the distortion of the potential surfaces in the substrate is clearly evident here.

While the comparisons of the potential surface in the plane of the particle track presented in Figs. 21 through 25 show both qualitative and quantitative agreement it must be recalled that the distortions associated with the two-dimensional result extend over the entire assumed device width. However, the three-dimensional disturbance may exhibit significant variation over the device width. To examine how far the disturbance caused by particle track extends in the third (y) dimension, the potential variation in two planes normal to the particle track is presented in Figs. 26 through 30 at five instants during the transient. In these figures the viewer is looking directly down the particle track, through the gate contact. Since the solution is symmetric about the z axis, only the top half of the device is shown in these figures. Thus, the particle track is centered at the bottom of the figures. In each figure, the left-hand frame represents the Y-Z plane $0.5 \mu\text{m}$ below the contact surface, just at the edge of the channel. The right-hand frame is for a Y-Z plane $8.24 \mu\text{m}$ below the contact surface, in the substrate. The source contact is on the right, and the drain is at the left of each frame. Note that in the channel region of the device the disturbance never extends much further than $2.5 \mu\text{m}$ outward from the track axis in the y direction. The nearly parallel, vertical potential contours indicate two-dimensionality, i.e., a lack of variation in the y direction. In the substrate, however, the result is somewhat different. In the absence of the particle track this plane would be at a constant potential. The particle track creates a disturbance which propagates radially outward from the track axis. Since there is no spatial variation of the donor or acceptor concentrations in the substrate, the disturbance is cylindrical about the track axis as opposed to the three-dimensional behavior observed in the active region of the device.

SECTION 5

SUMMARY AND CONCLUSIONS

The results of the present study show that the response of a typical GaAs JFET structure to single particle radiation entails a much more complex process than simple field funneling at the struck node. In the present study a JFET device, which is normally in the off state, was struck through the gate diffusion at normal incidence. However, the collection of charge at the gate was not augmented by the field funneling effect. Instead, a field funneling effect was set up between the gate and the N-channel, and the channel and the substrate drawing excess electrons into the channel to subsequently be collected at the drain. This was generated by a charge imbalance which resulted from the rapid collection of electrons from the gate depletion region while the holes, due to their lower transport coefficients and velocity saturation at the gate contact, were collected more slowly. The charge imbalance resulted in the distortion of the potential surface in an attempt to maintain charge neutrality. It appeared that this initial imbalance would remain constant for the duration of the event. However, a more significant aspect of the response was that the spreading of the excess charge throughout the substrate lowered the substrate resistance significantly and opened a source-drain current path in the off device. In essence, the presence of the N-channel blocked the collection of holes from the substrate and, in order to maintain a nearly charge-neutral state, electrons were injected at the source to replace those collected at the drain. There were, in effect, two components associated with the drain current. First, there was a small component of the drain current, balanced by a hole current at the gate, which accounted for collection of the excess carriers. As the results indicated, by 400psec this fraction of the drain current was very small. Second, there was the much larger portion of the drain current balanced by the source. This was similar to a typical FET current and was due to a modulation of the field in the channel and substrate by the spreading of the excess carriers. The simulations indicated that this would continue until the excess holes were collected. Since the excess carriers move through the substrate primarily by diffusion and since the holes must diffuse across the channel to the gate to be collected, the source-drain current flowed for a much longer time than that associated with the gate transient. The effect is exaggerated in GaAs due to the low diffusivity of holes. The present simulations indicated that this source-drain current could continue to flow 35nsec after the particle strike even though the gate transient was effectively over in 400psec.

In two previous studies [8,10] comparative two- and three-dimensional simulations of a silicon diode and an NMOS structure demonstrated that appropriate scaling of the charge density along an ion track in a two-dimensional simulation yielded a current pulse and charge collection rate that was in excellent qualitative and quantitative agreement with the three-dimensional results. Thus, it appeared that SEU simulations of such devices could be performed with reasonable confidence using the two-dimensional approach. The present study was undertaken to further verify such a scaling approach in a GaAs JFET. While the results of the present simulations showed qualitative agreement between the two- and three-dimensional JFET

simulations, quantitative differences in the current pulse at the device contacts and the resulting charge collection rate were observed. The peak current at the struck gate node was significantly lower in the three-dimensional simulation, by almost a factor of two. After 25psec however, the gate currents were almost identical in both cases. After 400psec, the gate current had decayed to less than 4% of the peak value. At that time the collected charge at the gate node was about 6% of the total ion generated charge in the two-dimensional case and about 5% in the three-dimensional case due to the lower peak current.

Significant differences were also observed in the resulting source-drain current which flows due to a lowering of the substrate resistance by the spreading of the excess carriers generated there. Here, the drain current did not rise to as high an initial peak in the three-dimensional simulation and the long term source-drain current level was somewhat lower.

After careful examination and comparison of the simulation results it was determined that the primary cause of the differences in the two- and three-dimensional results was a result of the device structure. Because of the shallowness of the p^+ gate diffusion, velocity saturation occurred at this contact, even before the particle strike, and the contact resistance is not constant but highly dependent, in a nonlinear fashion, on the field at this contact. In the two-dimensional case, the field distortions at this contact are uniform across the assumed device depth. However, in the three-dimensional case, only localized field distortions occur and the average contact resistance is different from the two-dimensional case, resulting in the observed difference in the current pulse at the gate contact. In the results reported in [8,10] the contact resistances were constant at all contacts. Thus it is concluded here that scaling of the track density in two-dimensional simulations will provide accurate results for current pulses and charge collection transients only if the contact resistances are constant. This, in effect, requires that the field at the contacts remain low enough to maintain operation in the constant mobility region of the velocity field relationship. Outside this range, while qualitatively accurate results may be obtained, the magnitude of any quantitative differences can only be accessed through accurate, three-dimensional simulations. It is therefore apparent that in the design of devices which are hardened against single particle radiation effects, two-dimensional simulation can provide a rapid and efficient means of exploring various device modifications and structural variations. However, once such a screening process is completed, the results of effective hardening approaches should be verified, at least selectively, using three-dimensional simulation where possible.

SECTION 6

LIST OF REFERENCES

1. Hsieh, C.M., Murley, P.C. and O'Brien, R.R.: A field-Funneling Effect on the Collection of Alpha-Particle-Generated Carriers in Silicon Devices, IEEE Electron Device Letters, April 1981. 2.
2. Grubin, H.L., Kreskovsky, J.P. and Weinberg, B.C.: Numerical Studies of Charge Collection and Funneling in Silicon Devices, IEEE Transactions on Nuclear Science, December 1984. 3.
3. Grubin, H.L., Kreskovsky, J.P. and Weinberg, B.C.: Theoretical Studies of Transient Electronic Effects in Silicon and Gallium Arsenide Devices Produced by a Single Heavily Ionized Track, SRA Report R82-940001-F, prepared for U.S. Defense Nuclear Agency.
4. Kreskovsky, J.P., and Grubin, H.L.: Simulation of Single Radiation Particle Tracks in Silicon and Gallium Arsenide Semiconductor Devices, DNA Tr-86-295, August 1986.
5. Kreskovsky, J.P. and Grubin, H.L.: Simulation of Charge Collection in a Multilayer Device, IEEE Transactions on Nuclear Science, December 1985.
6. Johnson, R.L., Diehl-Nagle, S.E. and Hauser, J.R.: Simulation Approach for Modeling Single Event Upsets on Advance CMOS SRAMS, IEEE Transactions on Nuclear Science, December 1985.
7. Fu, J.S., Weaver, H.T., Koga, R. and Kolasinski, W.A.: Comparison of ZD Memory SEU Transport Simulation With Experiments, IEEE Transactions on Nuclear Science, December 1985.
8. Kreskovsky, J.P. and Grubin, H.L.: Computation and Comparison of Charge Collection in Two- and Three-Dimensional Silicon Diodes, SRA Report R84-940003-F, August 1984.
9. Kreskovsky, J.P. and Grubin, H.L.: Numerical Simulation of Charge Collection in Two- and Three-Dimensional Silicon Diodes - A Comparison, Solid State Elec. Vol. 29, No. 5, 1986.
10. Kreskovsky, J.P., Grubin, H.L., and Morrison, B.J.: Two- and Three-Dimensional Simulation of Silicon NMOS Device Response to Single Particle Radiation Using a Vectorized Solution Algorithm, SRA Report R87-940006-F, March 1987.
11. Buturla, E.M., Cottrell, P.E., Grossman, B.M., McMullen, C.T. and Salsburg: Three-dimensional Transient Finite Element Analysis of Semiconductor Transport Equations, in Numerical Analysis of Semiconductor Devices and Integrated Circuits, Boole Press, 1981.
12. Lundstrom, M.S. and Schuelke, R.J.: Modeling Semiconductor Heterojunctions in Equilibrium, Solid State Electronics, 1982.

LIST OF REFERENCES (continued)

13. Sze, S.M.: Physics of Semiconductor Devices, Wiley - Interscience, 1969.
14. Blakemore, J.S.: Semiconducting and Other Major Properties of Gallium Arsenide, J. App. Phy., Vol. 53, No. 10, October 1982.
15. Kreskovsky, J.P. and Grubin, H.L.: Application of LBI Techniques to the Solution of the Transient, Multi-dimensional Semiconductor Equations, Journal of Computational Physics, 1987.
16. Briley, W.R. and McDonald, H.: Solution of the Multi-dimensional Compressible Navier-Stokes Equations by a Generalized Implicit Method, Journal of Computational Physics, August 1977.
17. Douglas, J. and Gunn, J.E.: A General Formulation of Alternating Direction Methods, Part I. Parabolic and Hyperbolic Problems, Numerische Mathematik, Vol. 6, 1964.
18. Yaney, D.S., Nelson, J.T. and Vanskike, L.L.: Alpha Particle Tracks in Silicon and Their Effect on Dynamic MOS RAM Reliability, IEEE Transactions on Electron Devices, 1979.

TABLE 1

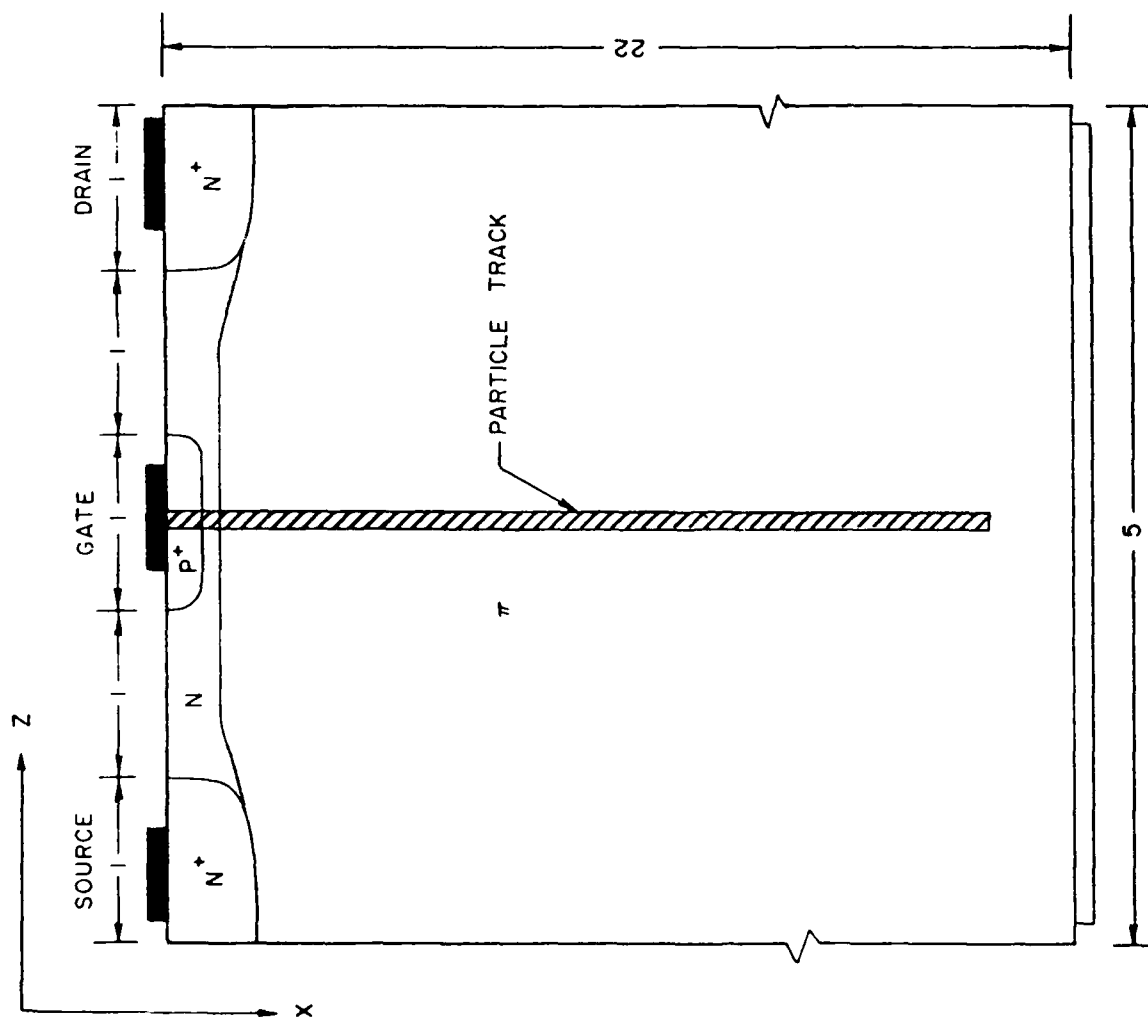
AVALANCHE GENERATION COEFFICIENTS

<u>PARAMETER</u>	<u>GALLIUM ARSENIDE VALUE</u>
A_n	1.90×10^5
A_p	2.21×10^5
b_n	5.75×10^5
b_p	6.57×10^5
m_n	1.75
m_p	1.75

TABLE 2

MOBILITY PARAMETERS FOR GALLIUM ARSENIDE

<u>PARAMETER</u>	<u>ELECTRON VALUE</u>	<u>HOLE VALUE</u>
a (cm/s)	1.0×10^6	----
b (cm/s)	6.0×10^6	----
c (cm/s)	7.5×10^6	----
E_v (volts/cm)	4.0×10^3	----
V_{sat} (cm/s)	----	1.0×10^7
β	----	2
μ_0 (cm ² /volt)	density dependent	200



NOTE

- 1) ALL DIMENSIONS
IN MICRONS
- 2) 3-D DEVICE IS
25 μm WIDE
- 3) THE Y DIRECTION
IS OUTWARD
NORMAL TO PAGE

Figure 1. Schematic representation of the JFET device considered showing the location of the particle strike.

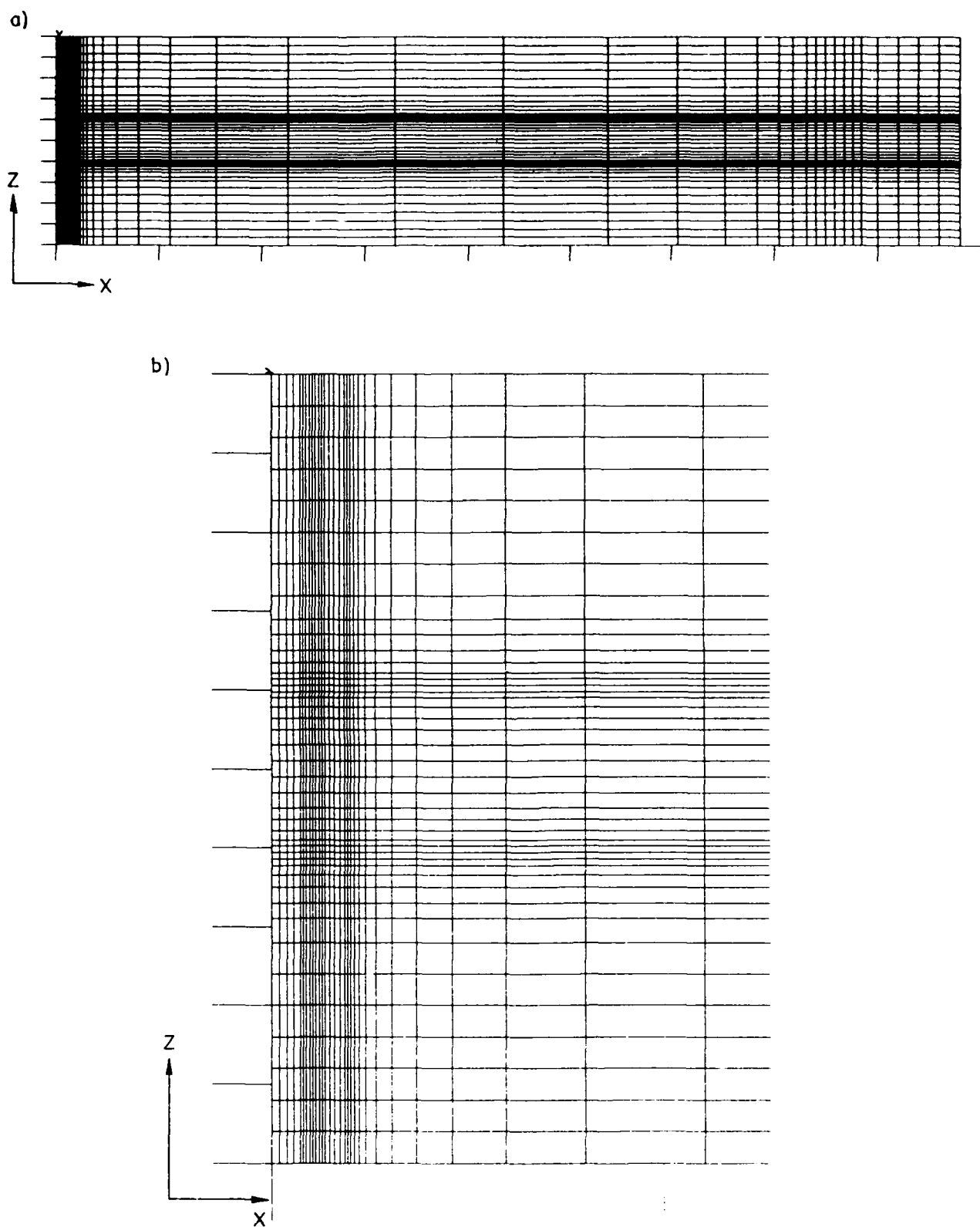


Figure 2. Grid in X-Z plane, a, and blow up of grid in the channel region, b.

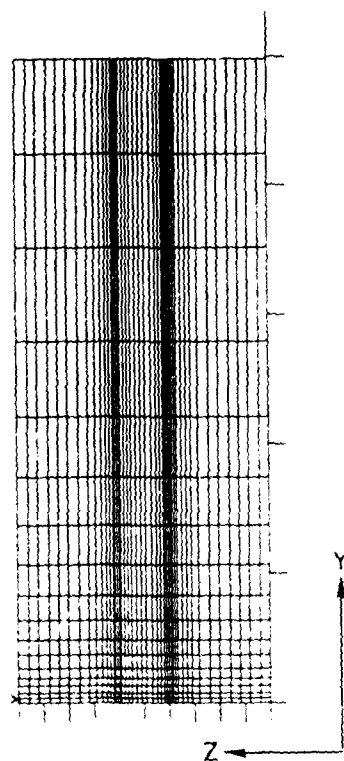
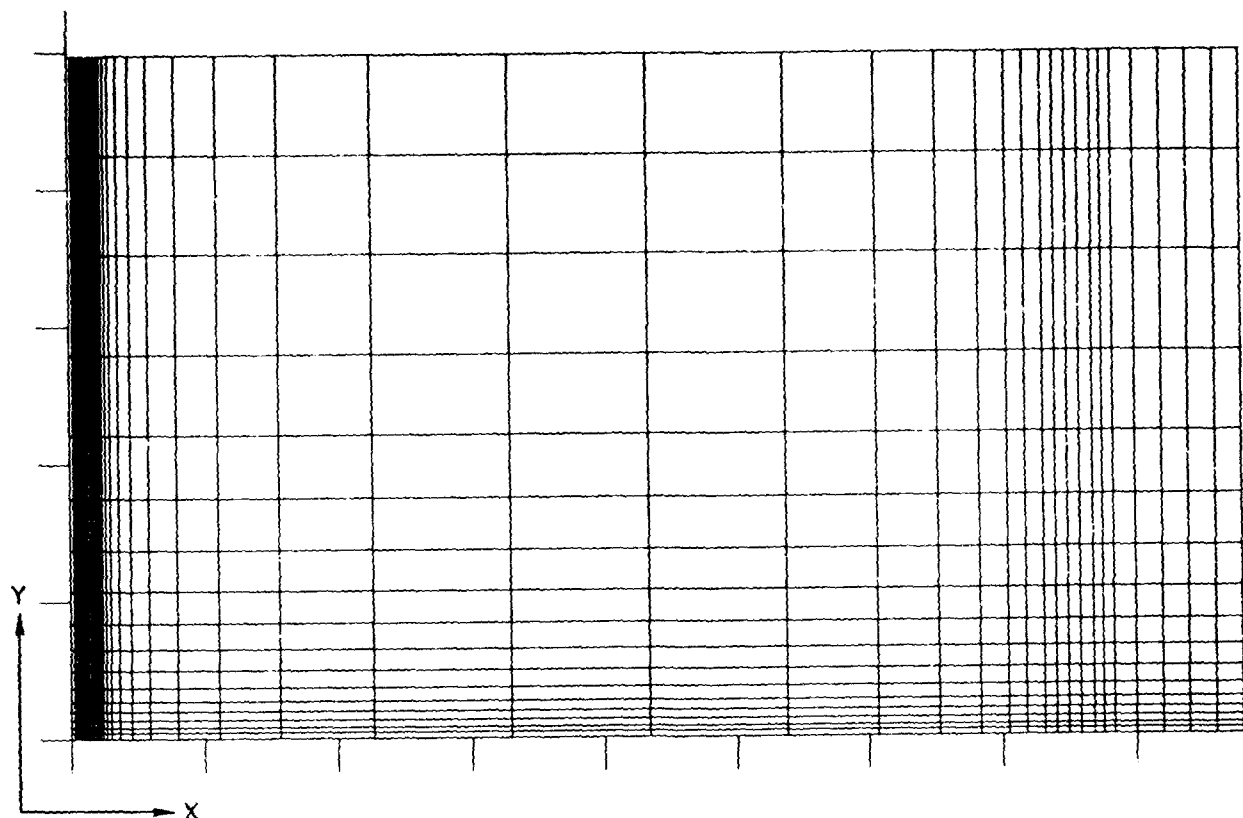


Figure 3. Grids in the X-Y and Y-Z planes as in the three-dimensional simulation.

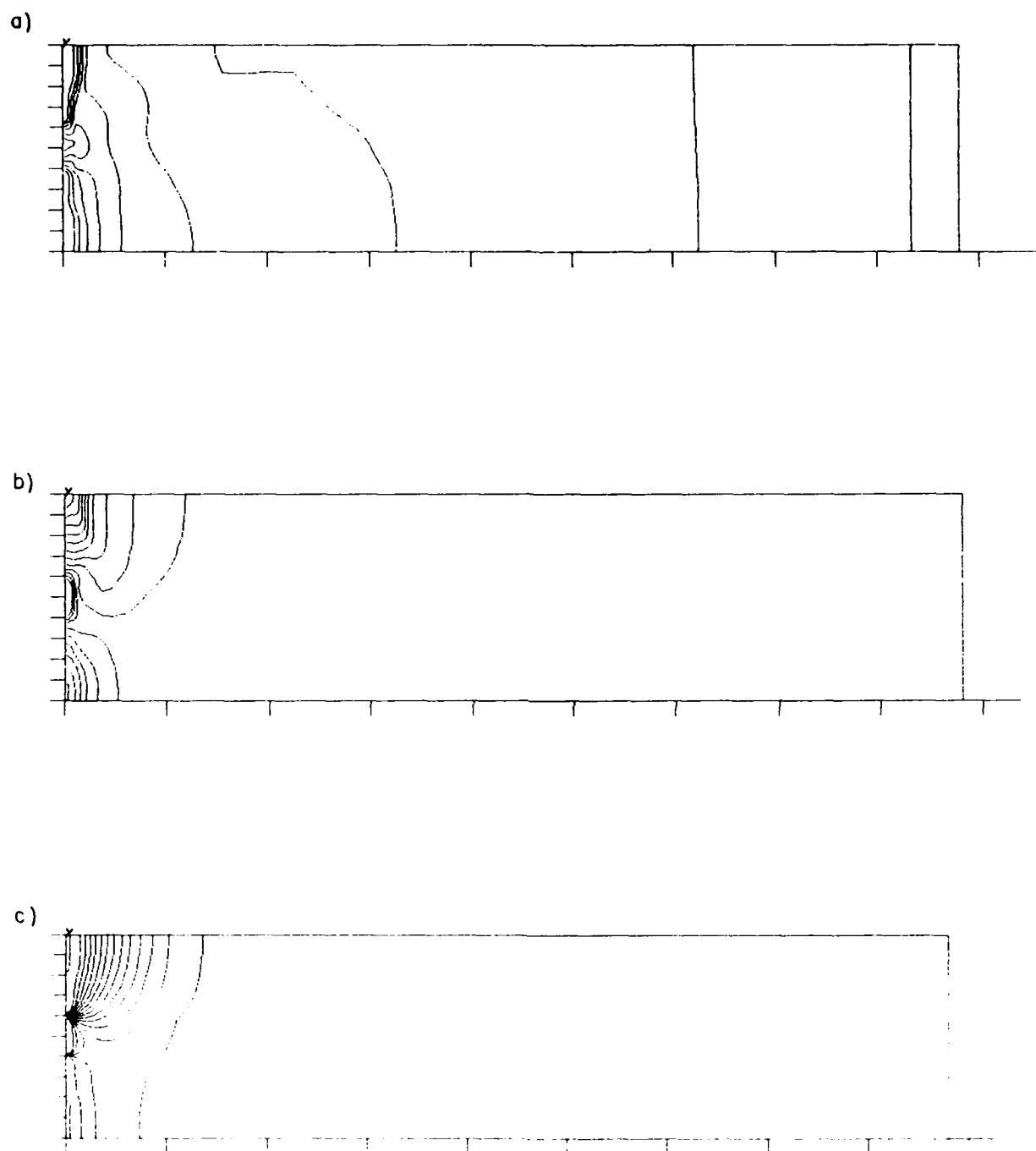


Figure 4. Steady state contours of a) $\log N$, b) $\log P$ and c) potential in the JFET.

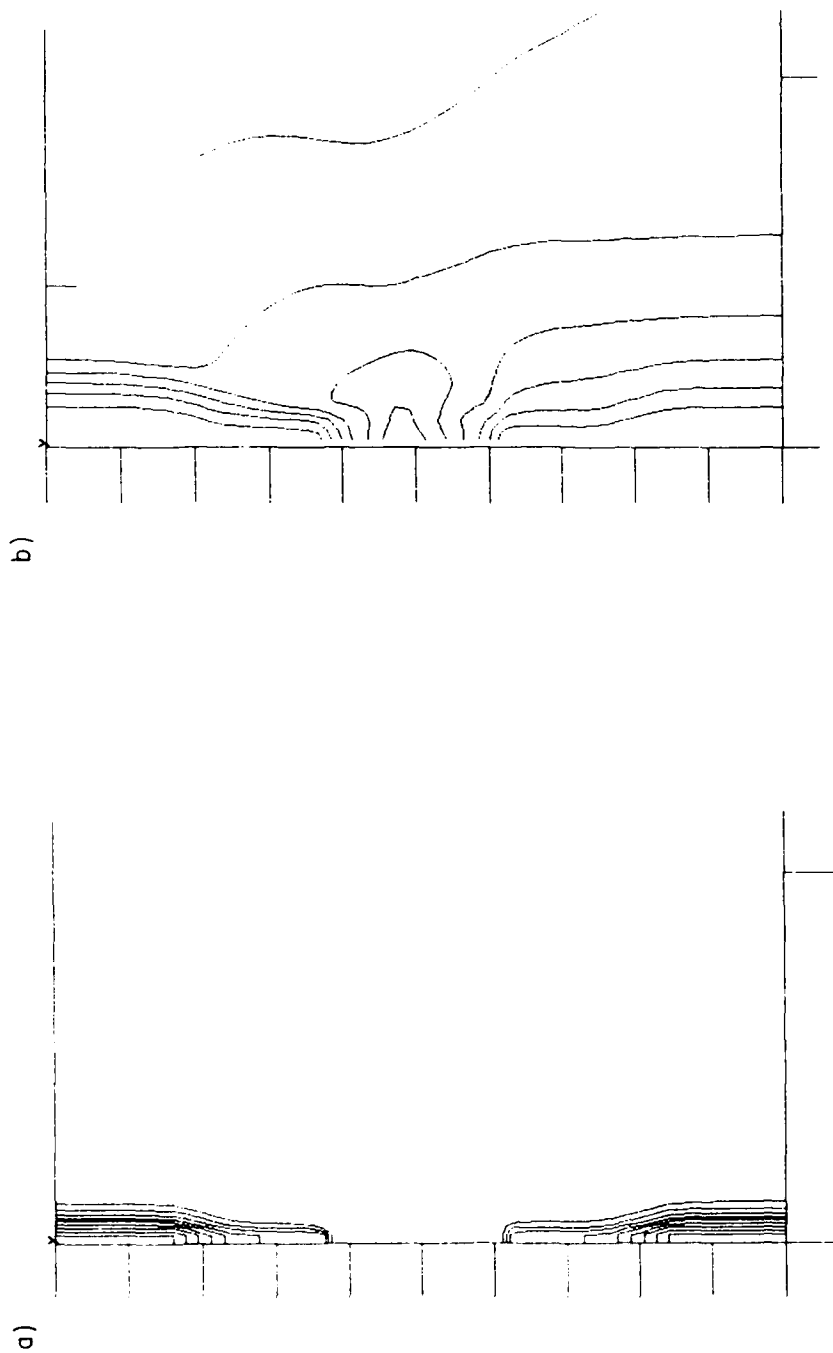


Figure 5 Steady state contours of electron density in the channel region of the JFET. a) contours of N , b) contours of $\log N$.

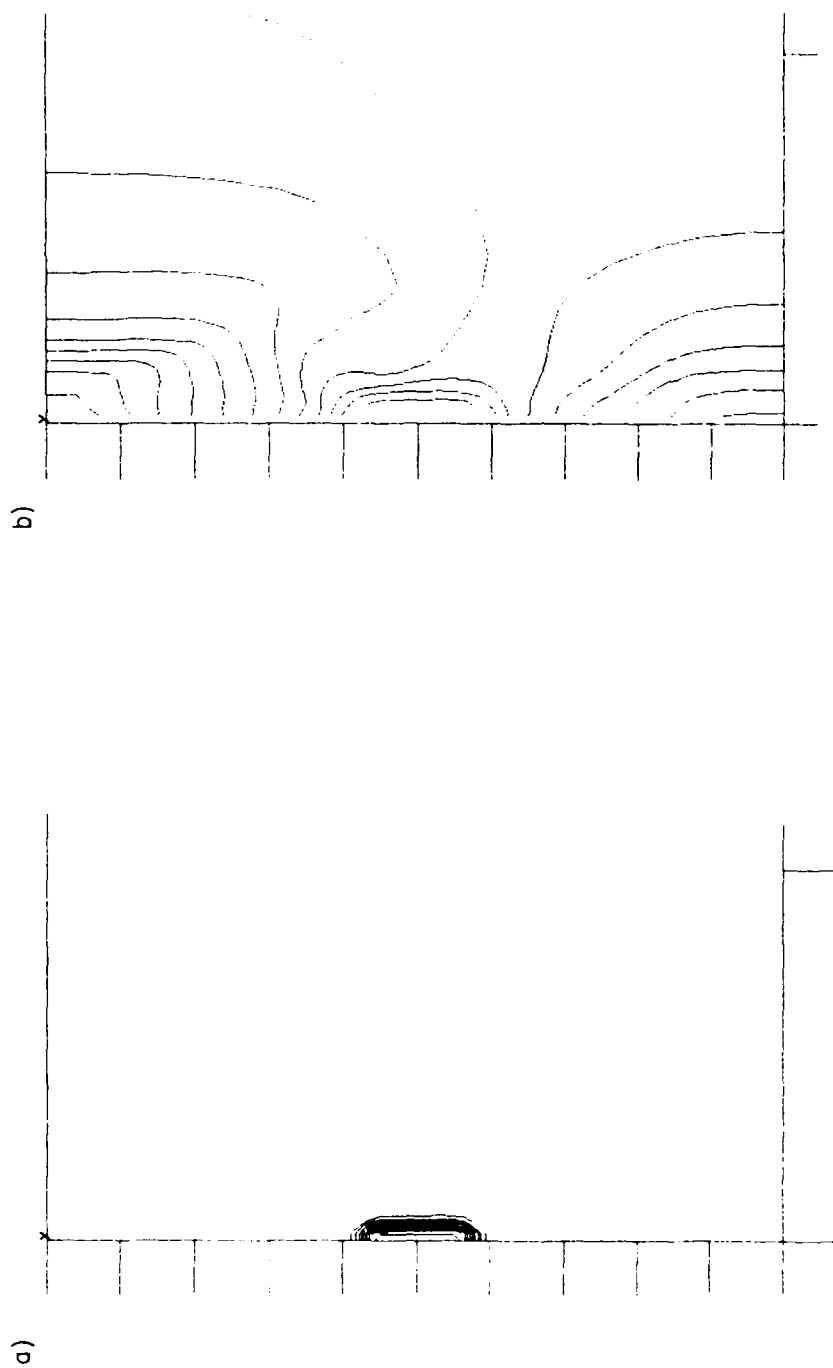


Figure 6. Steady state contours of hole density in the channel region of the JFET. a) contours of P , b) contours of $\log P$.

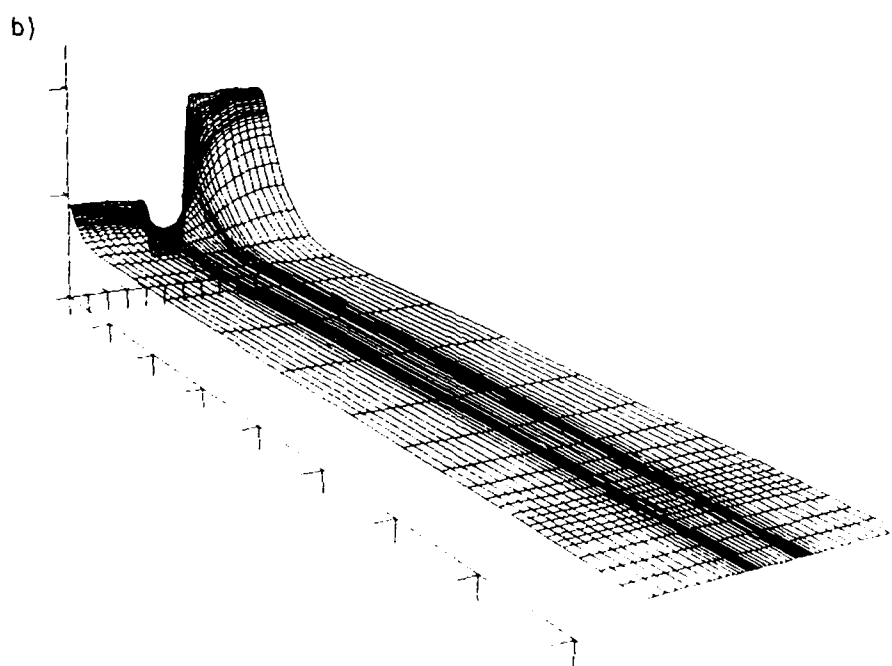
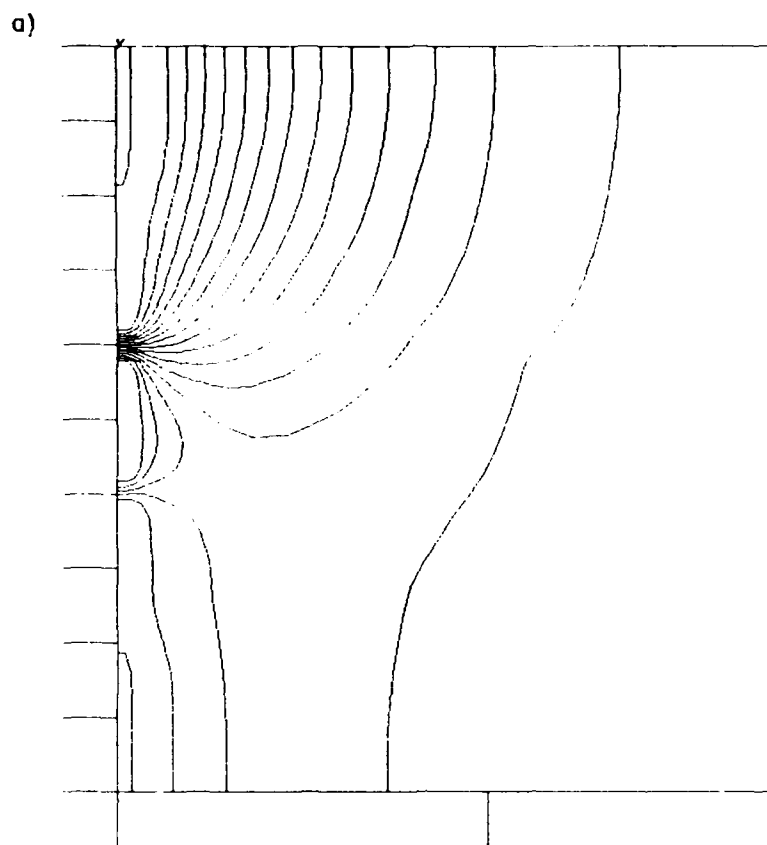


Figure 7. Steady state contours (a) and surface plot (b) of the potential in the JFET.

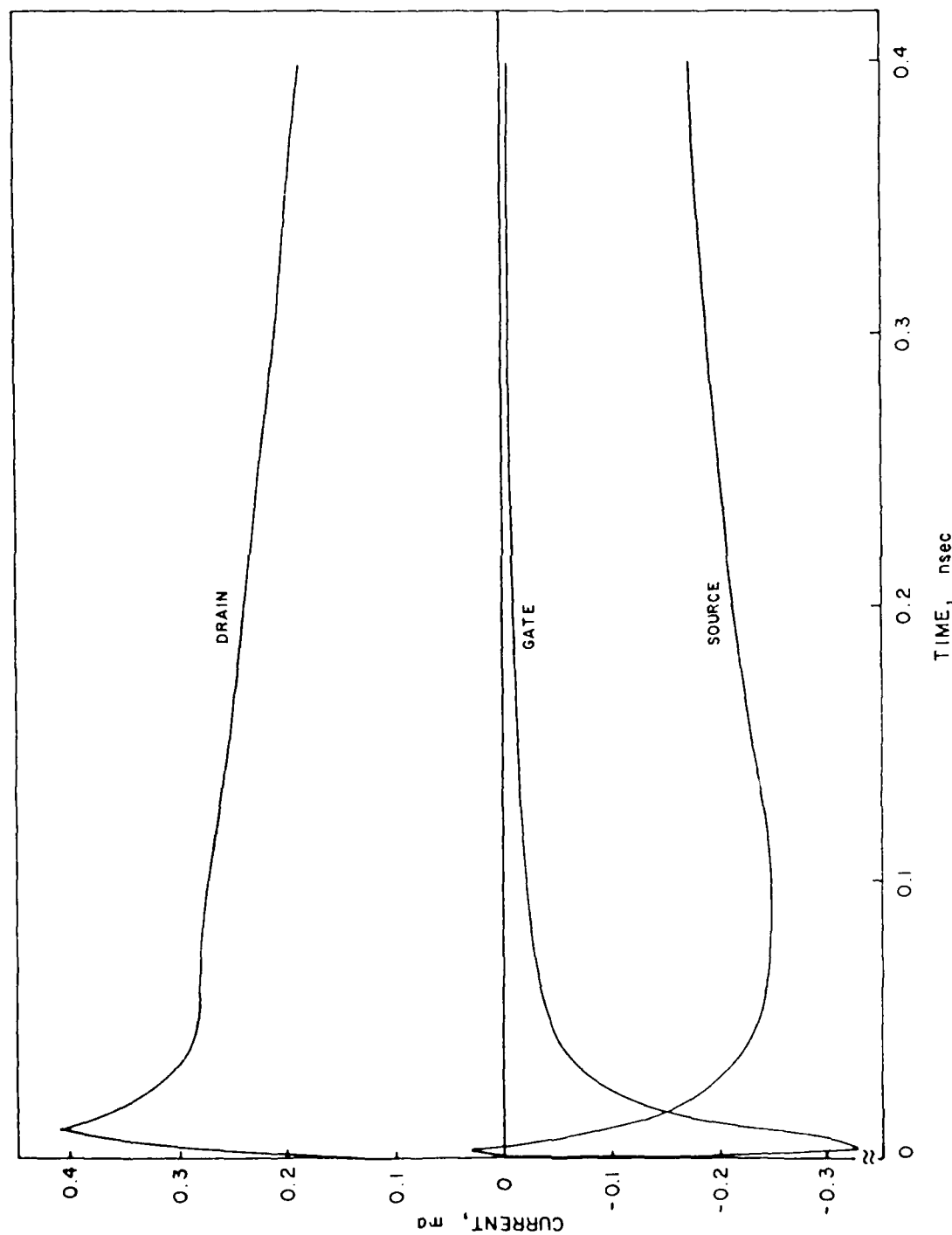


Figure 8. Current pulses as a function of time at source, drain and gate contacts after particle strike, 2-D result.

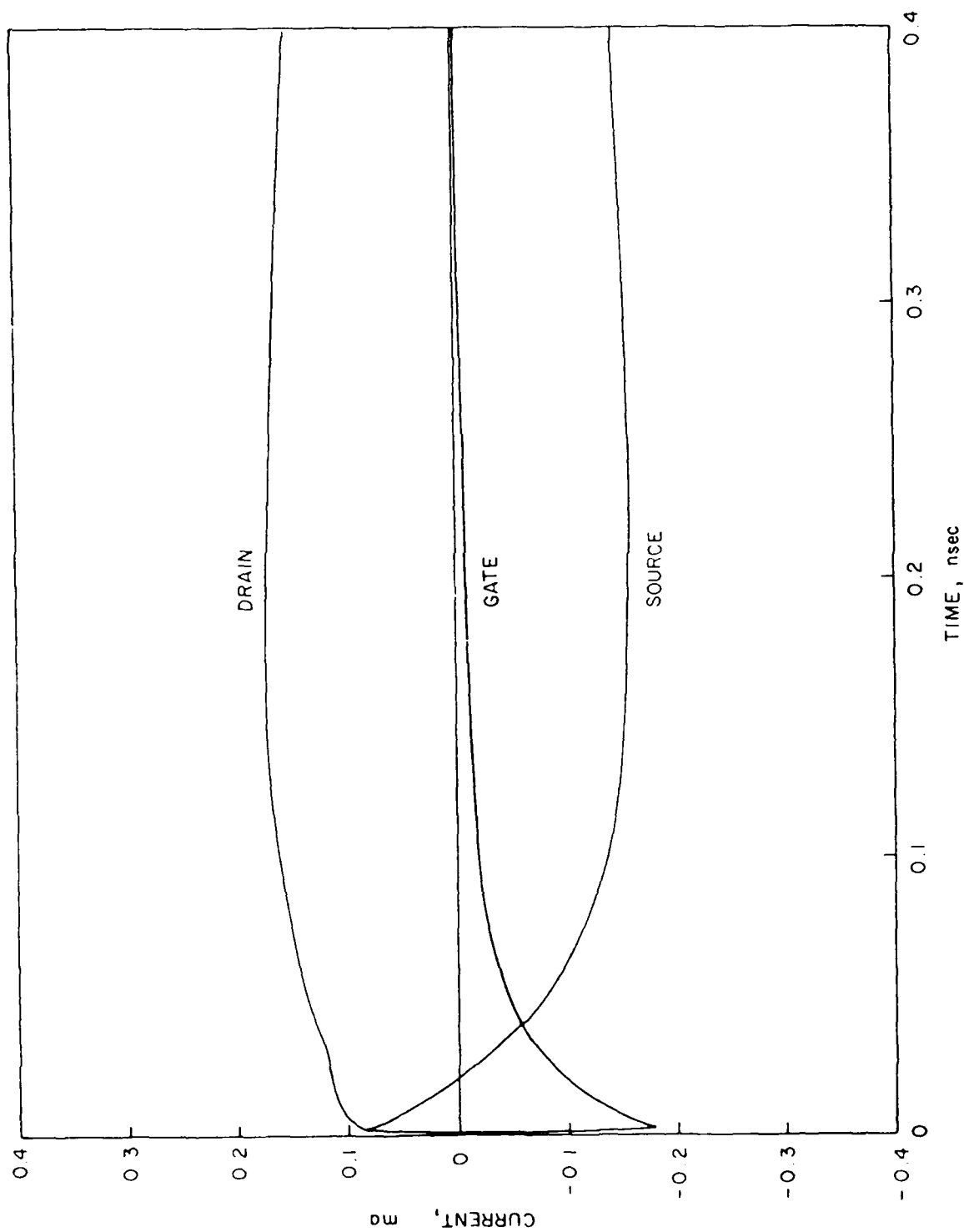


Figure 9. Current pulses as a function of time at source, drain and gate contacts after particle strike, 3-D result.

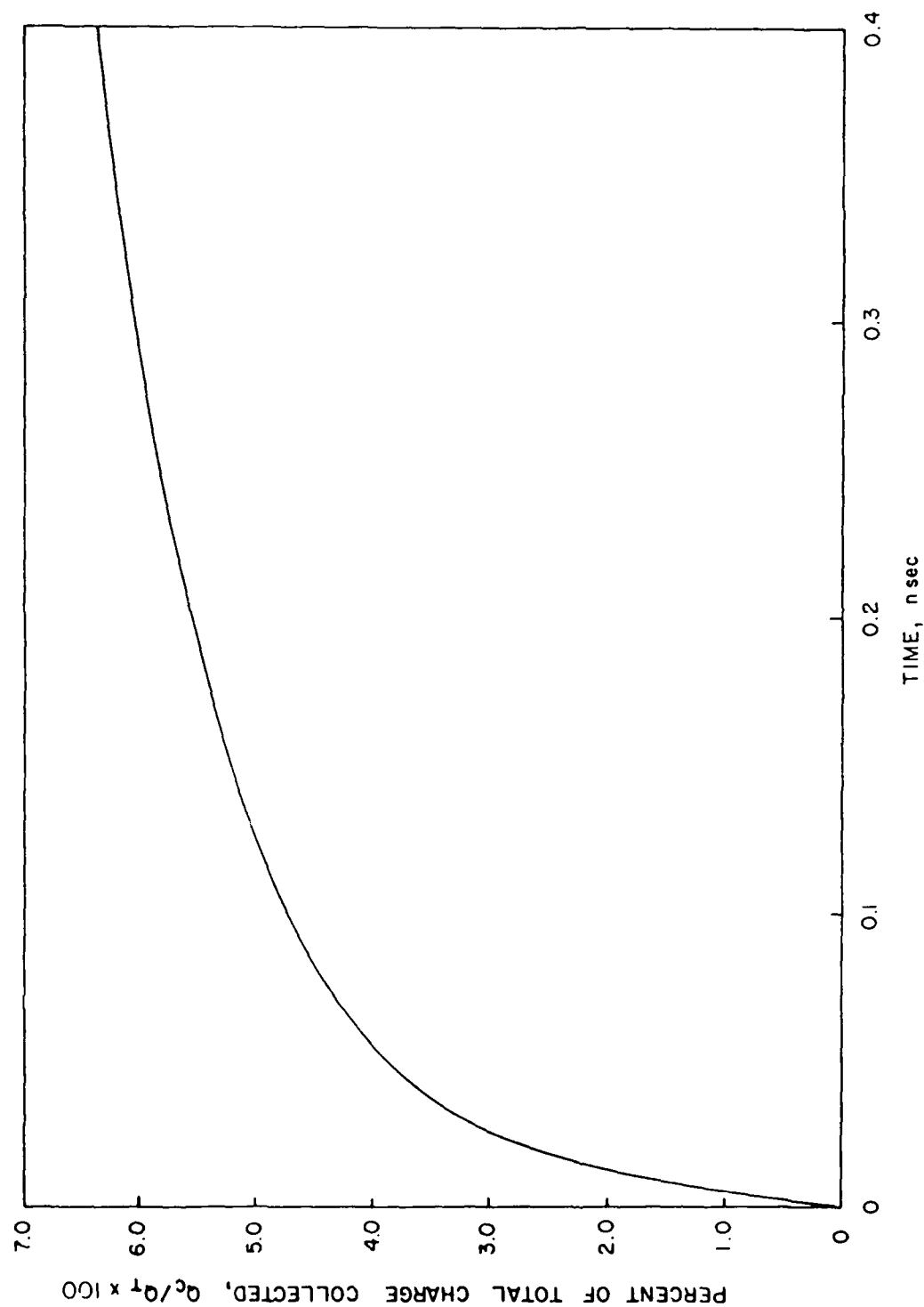


Figure 10. Percent of total particle generated charge collected at gate contact for 2-D simulation.

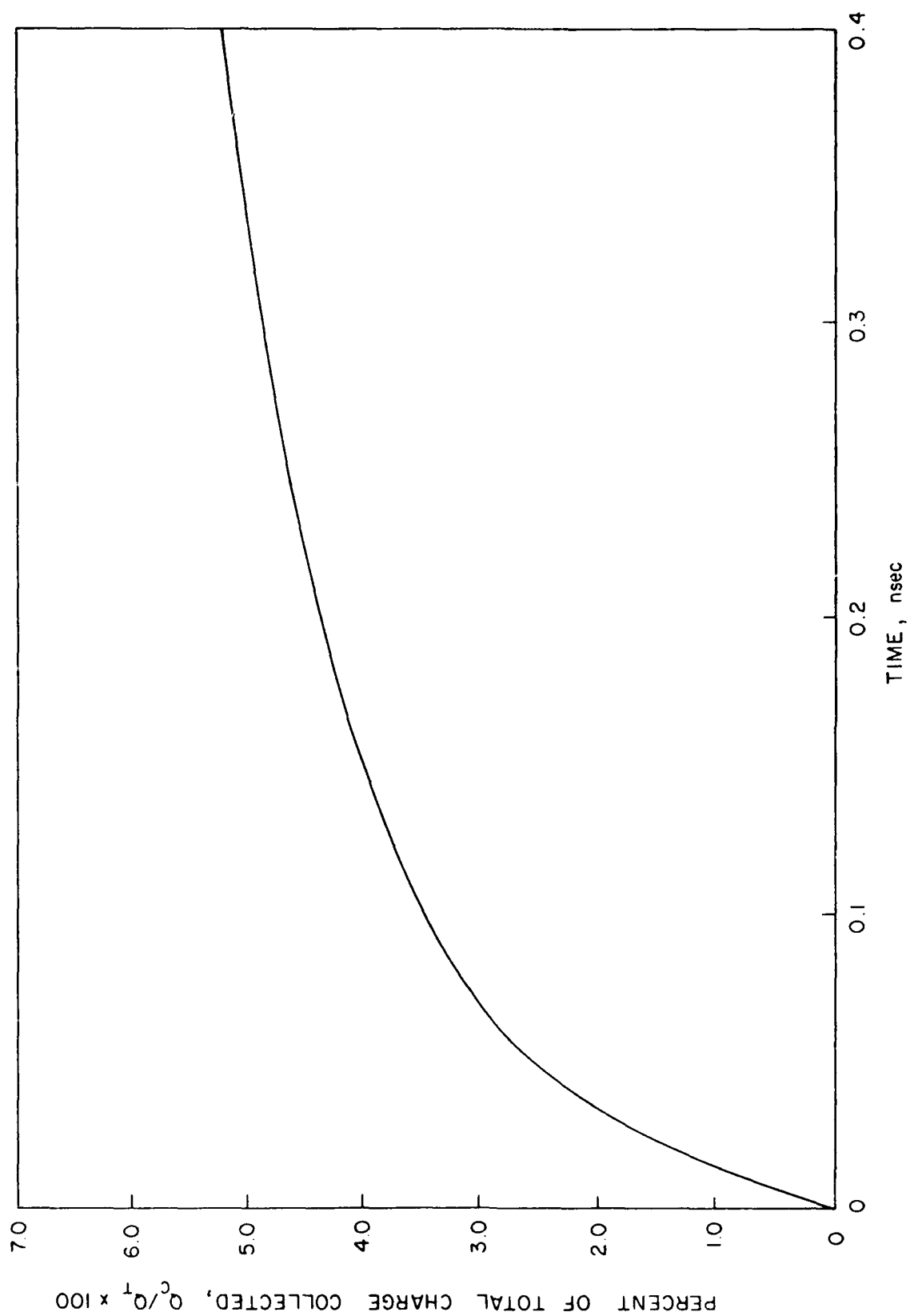


Figure 11. Percent of total particle generated charge collected at gate contact for 3-D simulation.

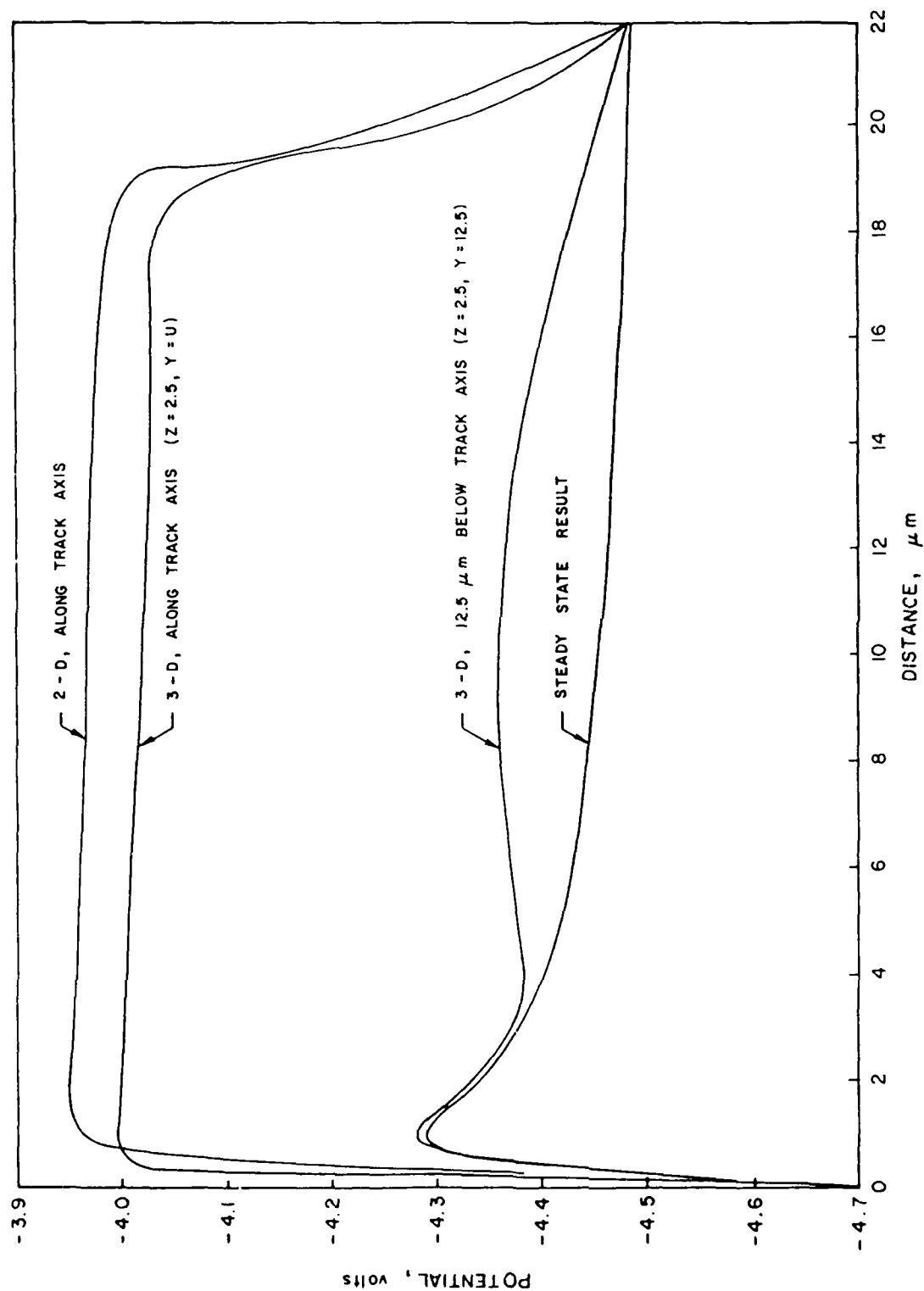


Figure 12. Comparison of potential distributions along the track axis for the 2-D and 3-D simulations with the steady state result and the 3-D result 12.5 μ m below the track axis 40 psec following the particle strike.

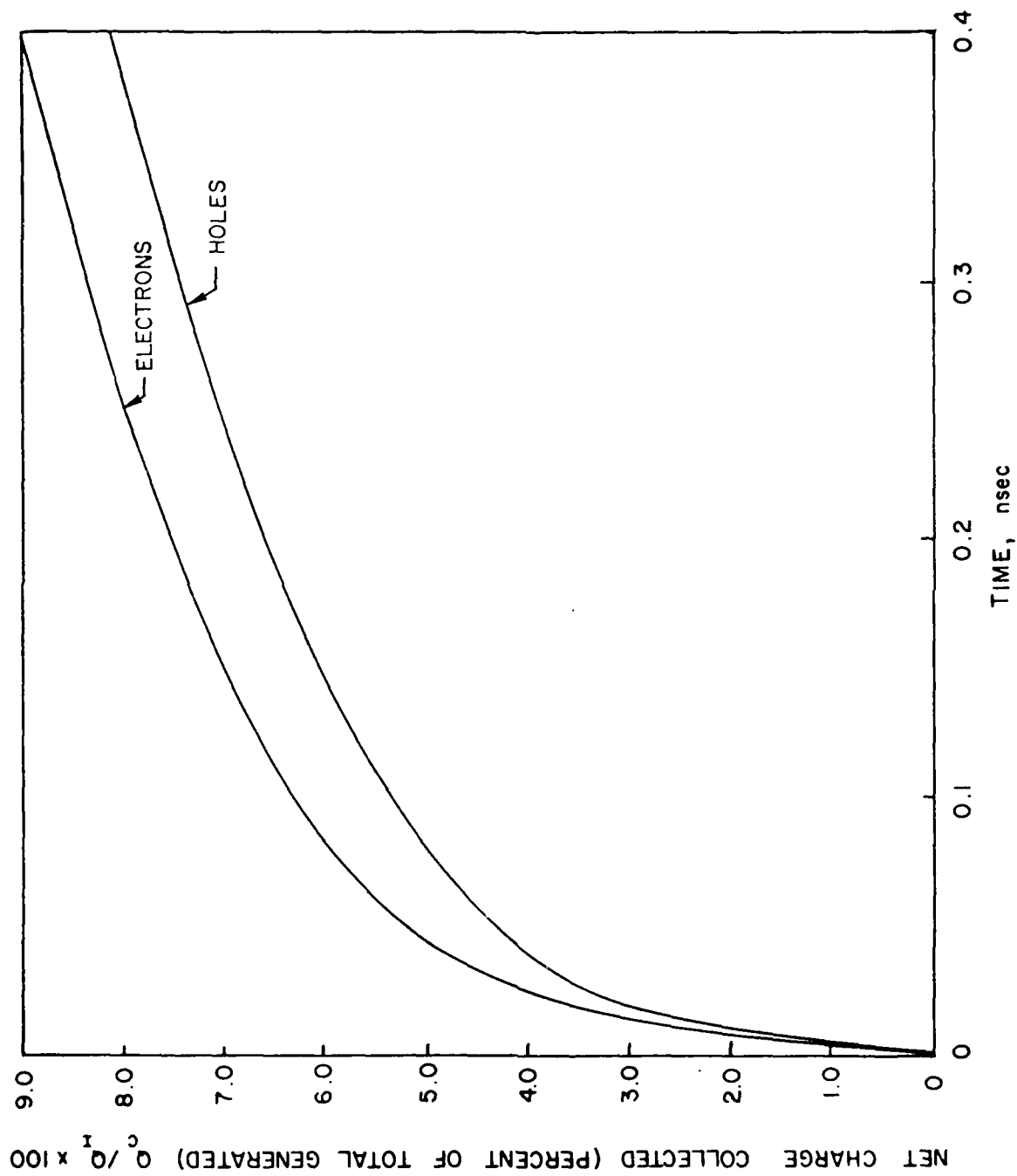


Figure 13. Net electron and hole charge collected at all contacts, 2-D result.

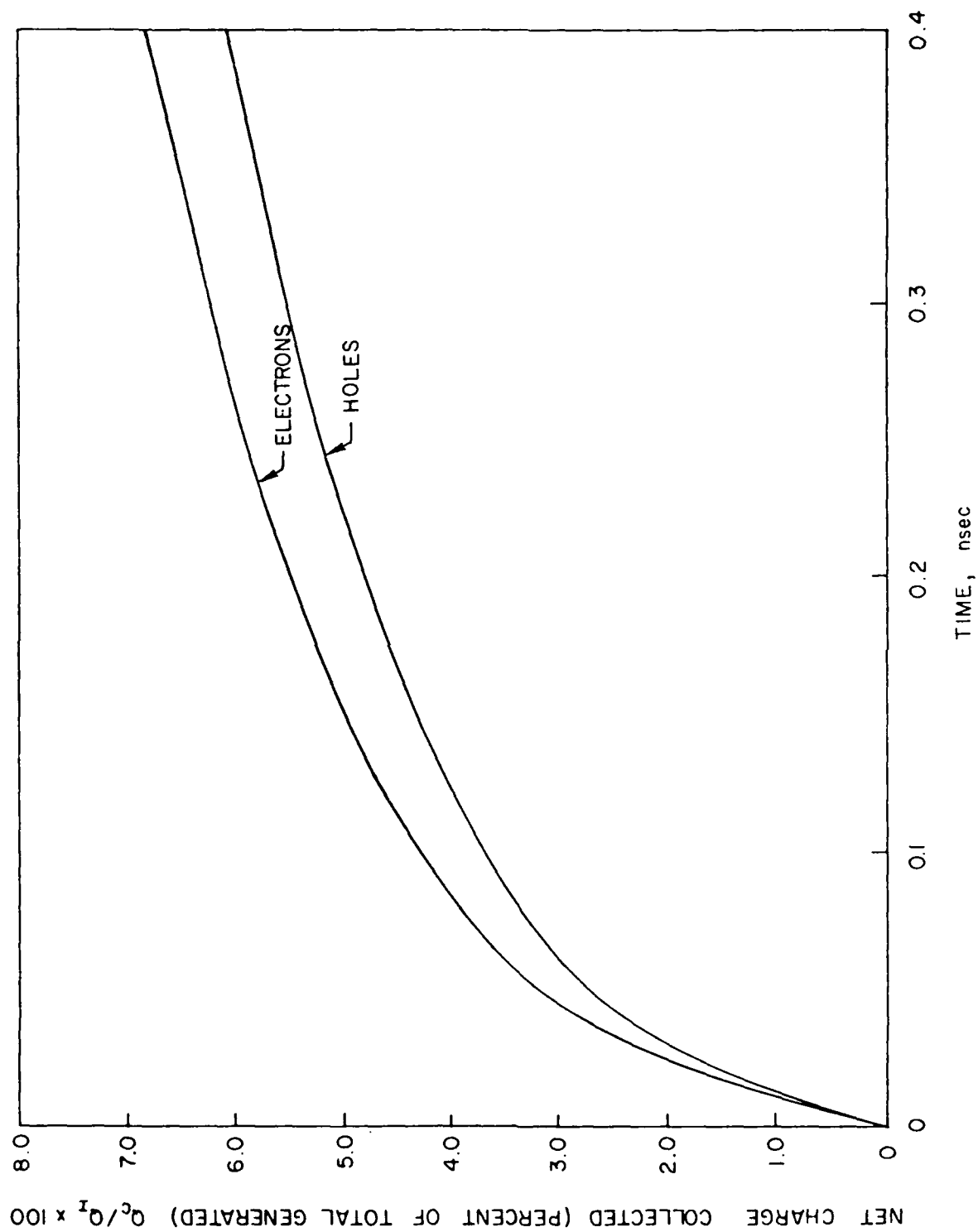


Figure 14. Net electron and hole charge collected at all contacts, 3-D result.

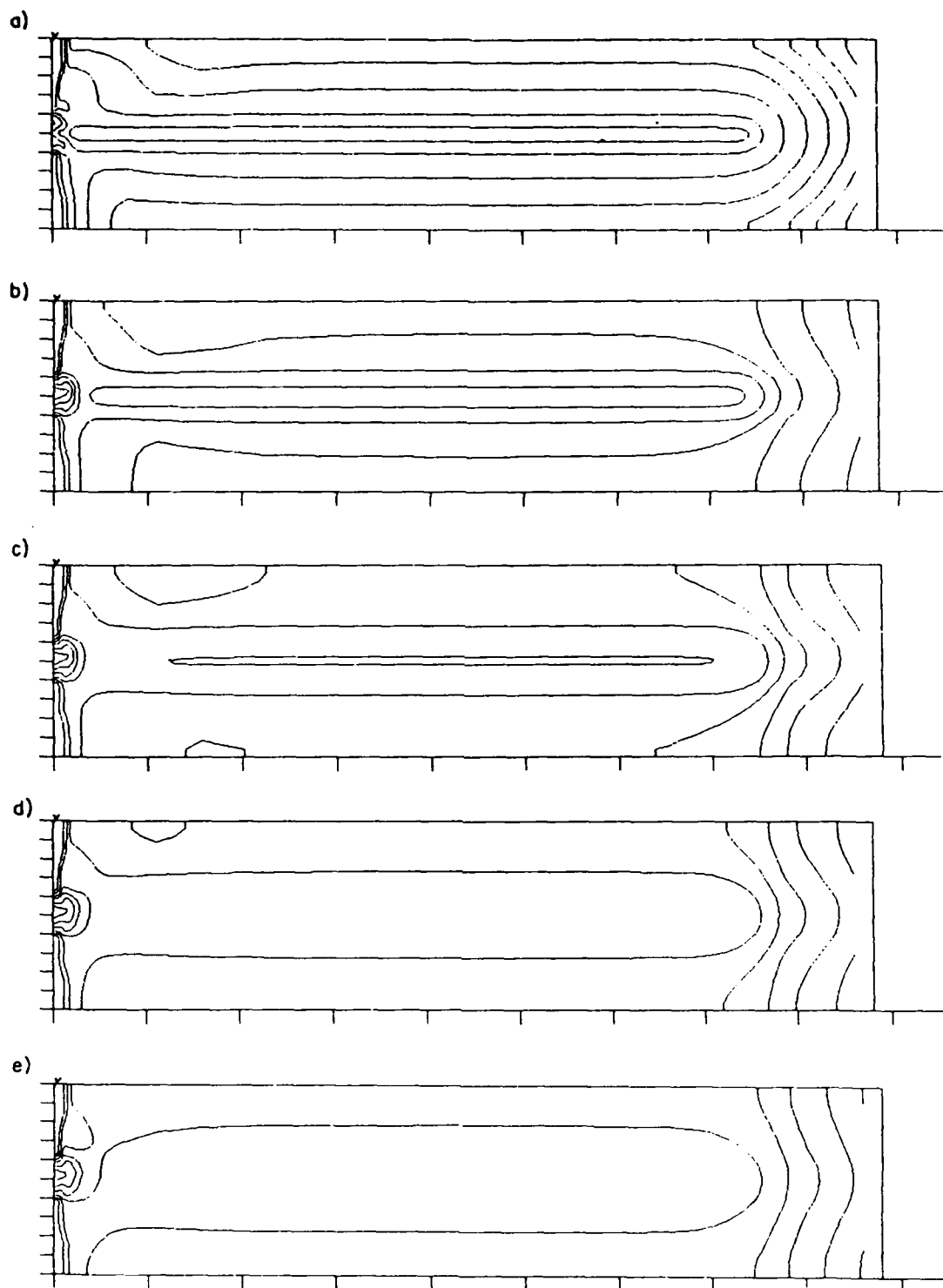


Figure 15. Contours of $\log N$ at a) 10 psec, b) 40 psec, c) 100 psec, d) 200 psec, and e) 400 psec following the particle strike for the 2-D case.

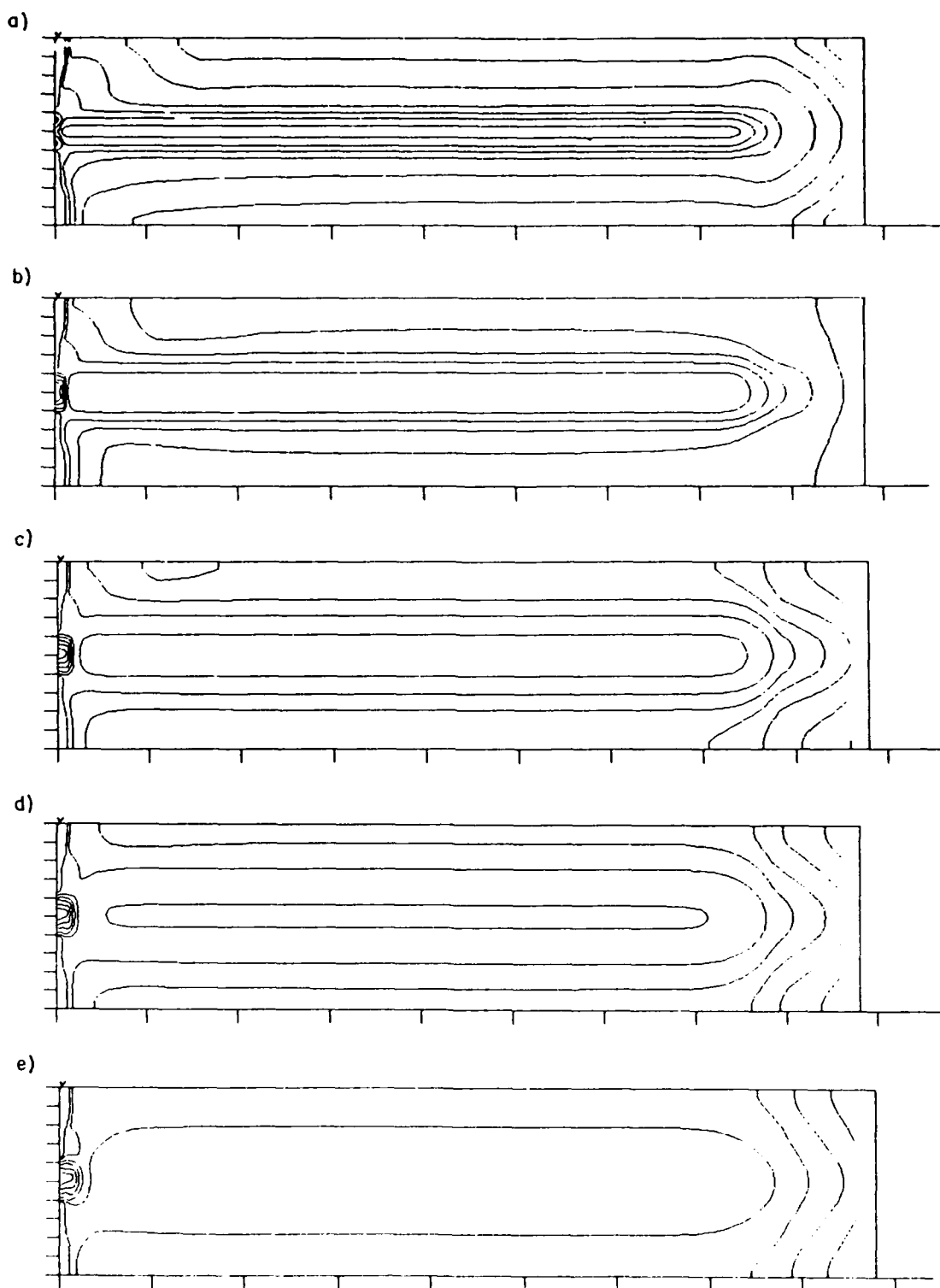


Figure 16. Contours of $\log N$ at a) 10 psec, b) 40 psec, c) 100 psec, d) 200 psec, and e) 400 psec following the particle strike for the 3-D case in the X-Z plane of the particle track.

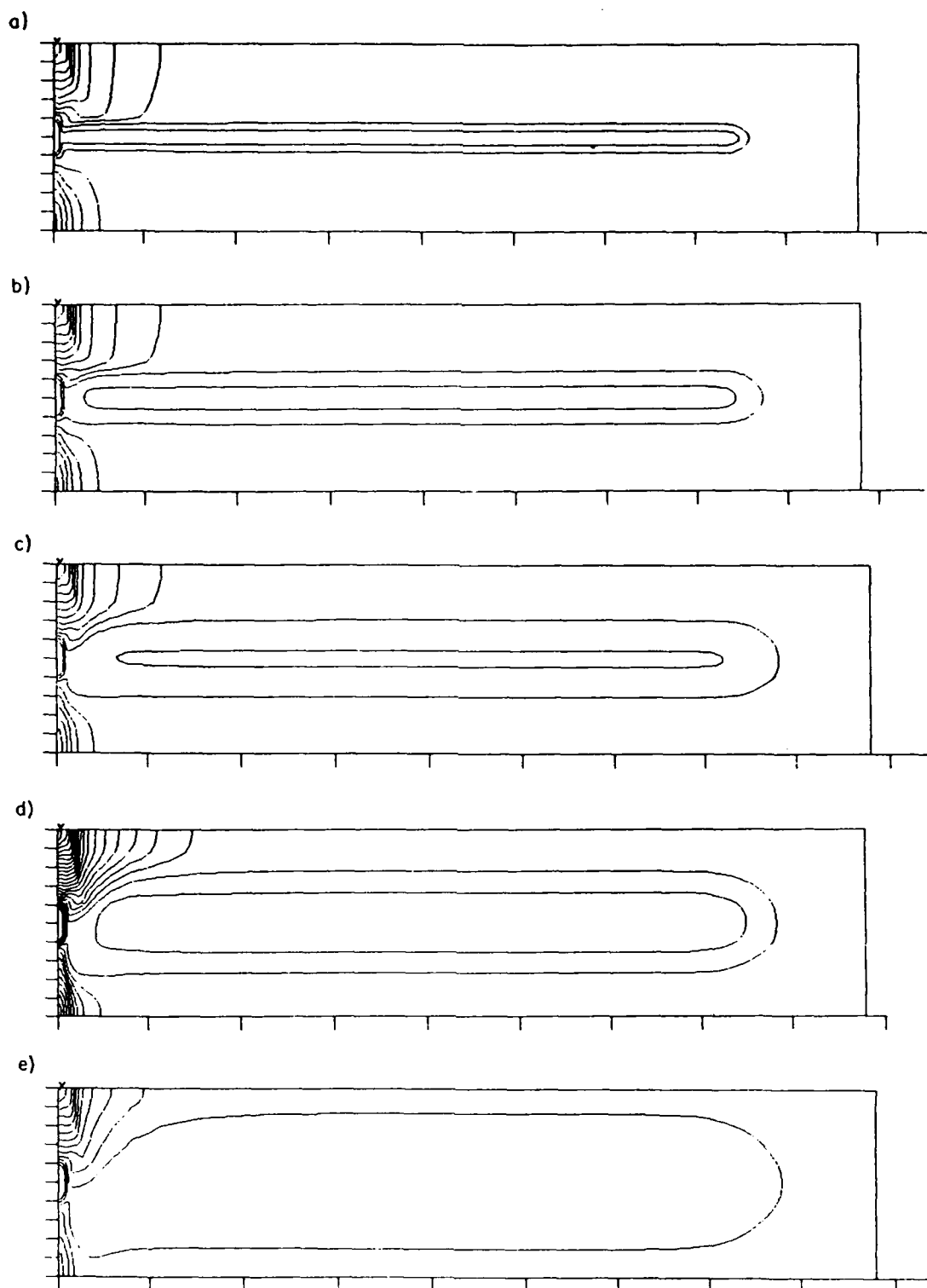


Figure 17. Contours of $\log P$ at a) 10 psec, b) 40 psec, c) 100 psec, d) 200 psec, and e) 400 psec following the particle strike for the 2-D case.

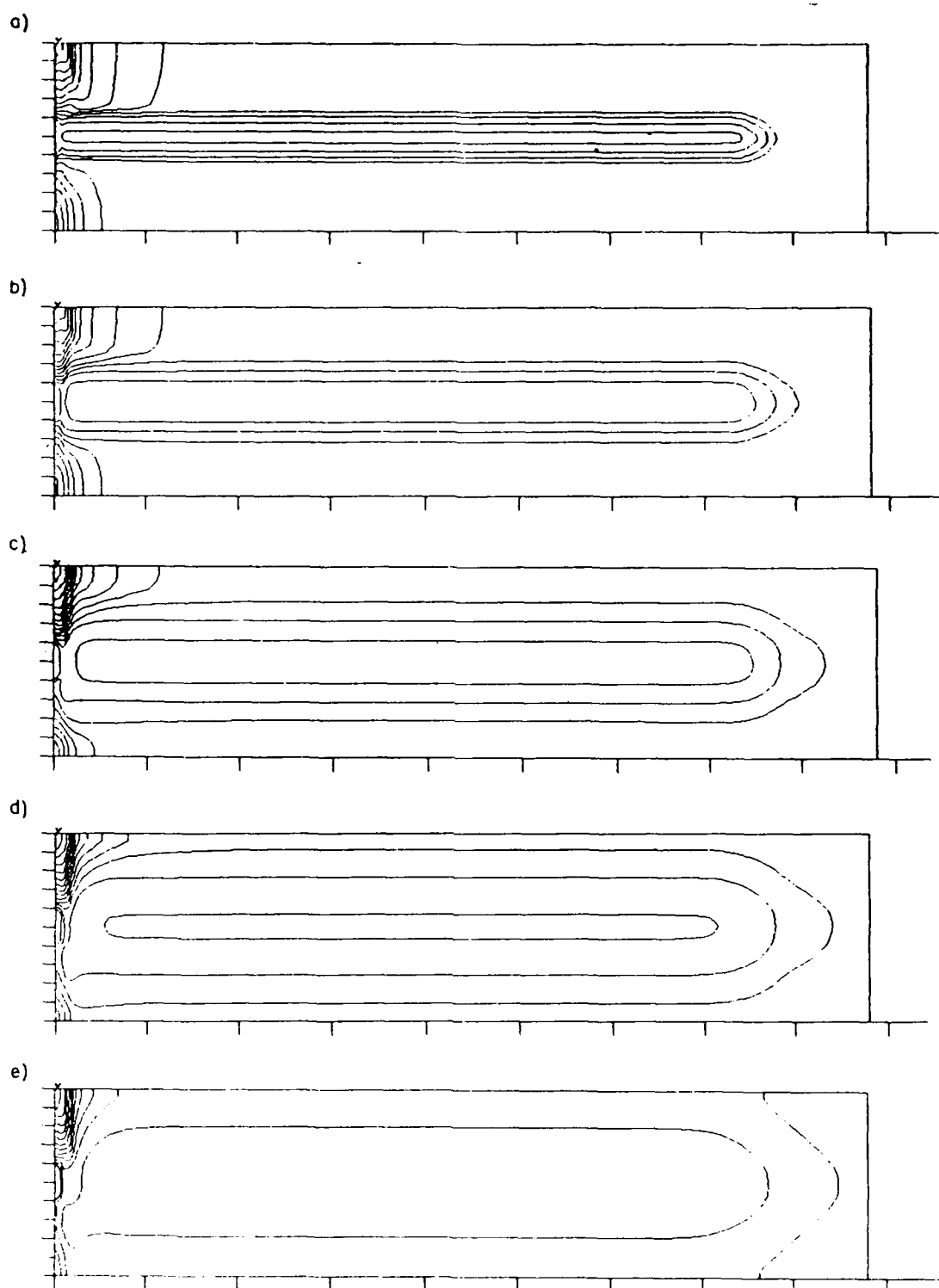


Figure 18. Contours of $\log P$ at a) 10 psec, b) 40 psec, c) 100 psec, d) 200 psec, and e) 400 psec following the particle strike for the 3-D case in the X-Z plane of the particle track.

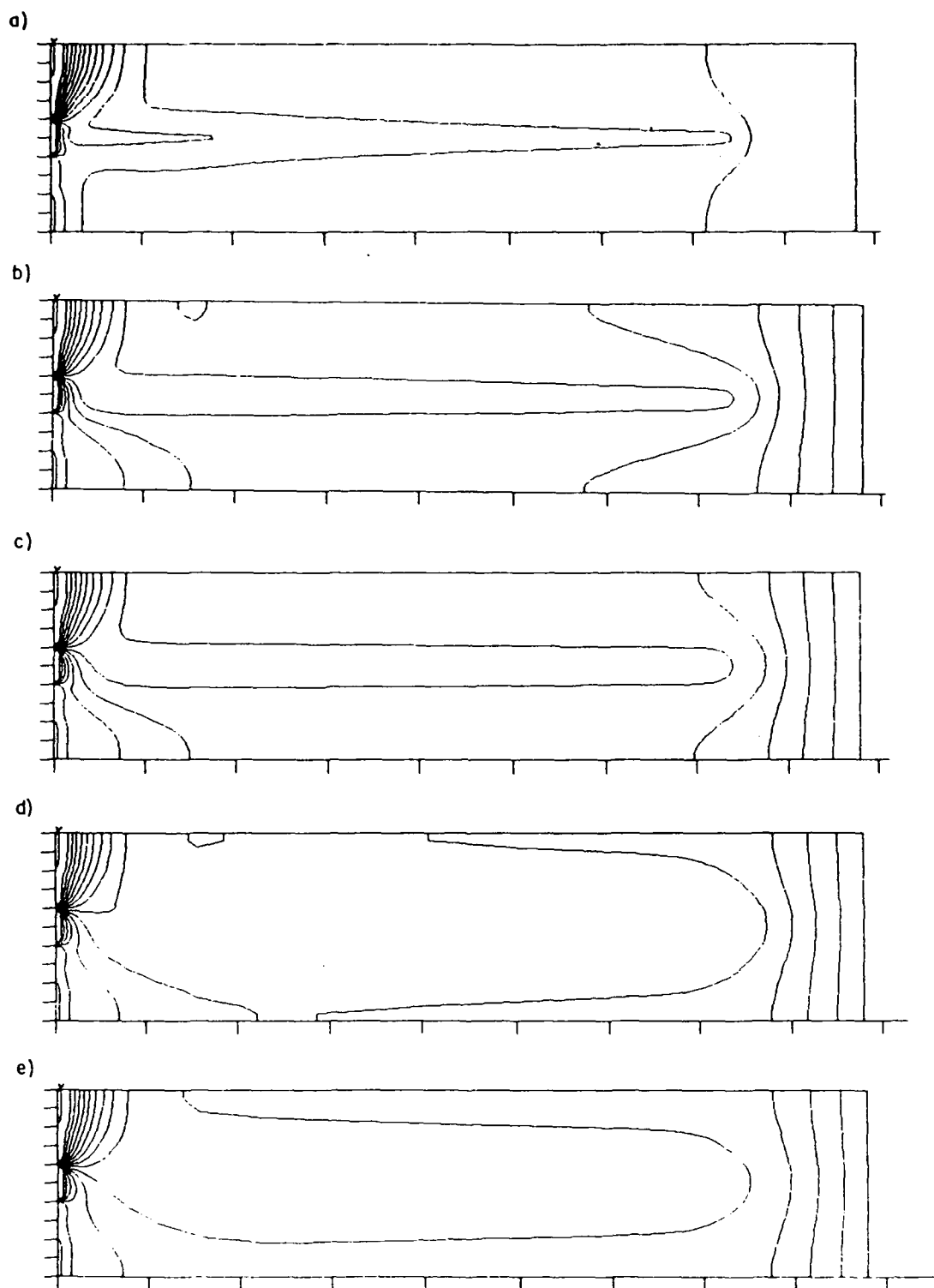


Figure 19. Contours of equa-potential at a) 10 psec, b) 40 psec, c) 100 psec, d) 200 psec and e) 400 psec following the the particle strike for the 2-D case.

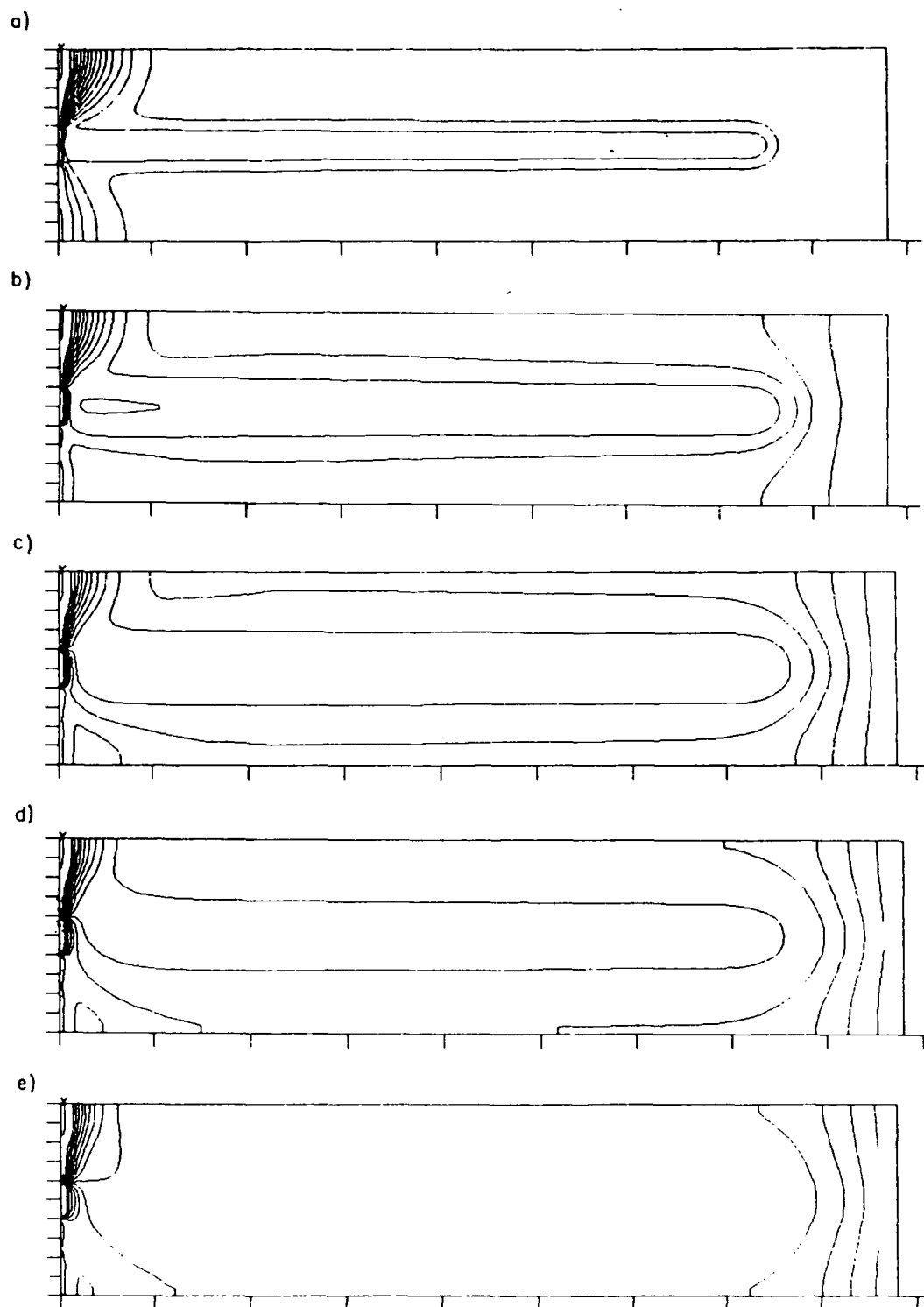


Figure 20. Contours of equa-potential at a) 10 psec, b) 40 psec, c) 100 psec, d) 200 psec and e) 400 psec following the particle strike for the 3-D case in the X-Z plane of the particle track.

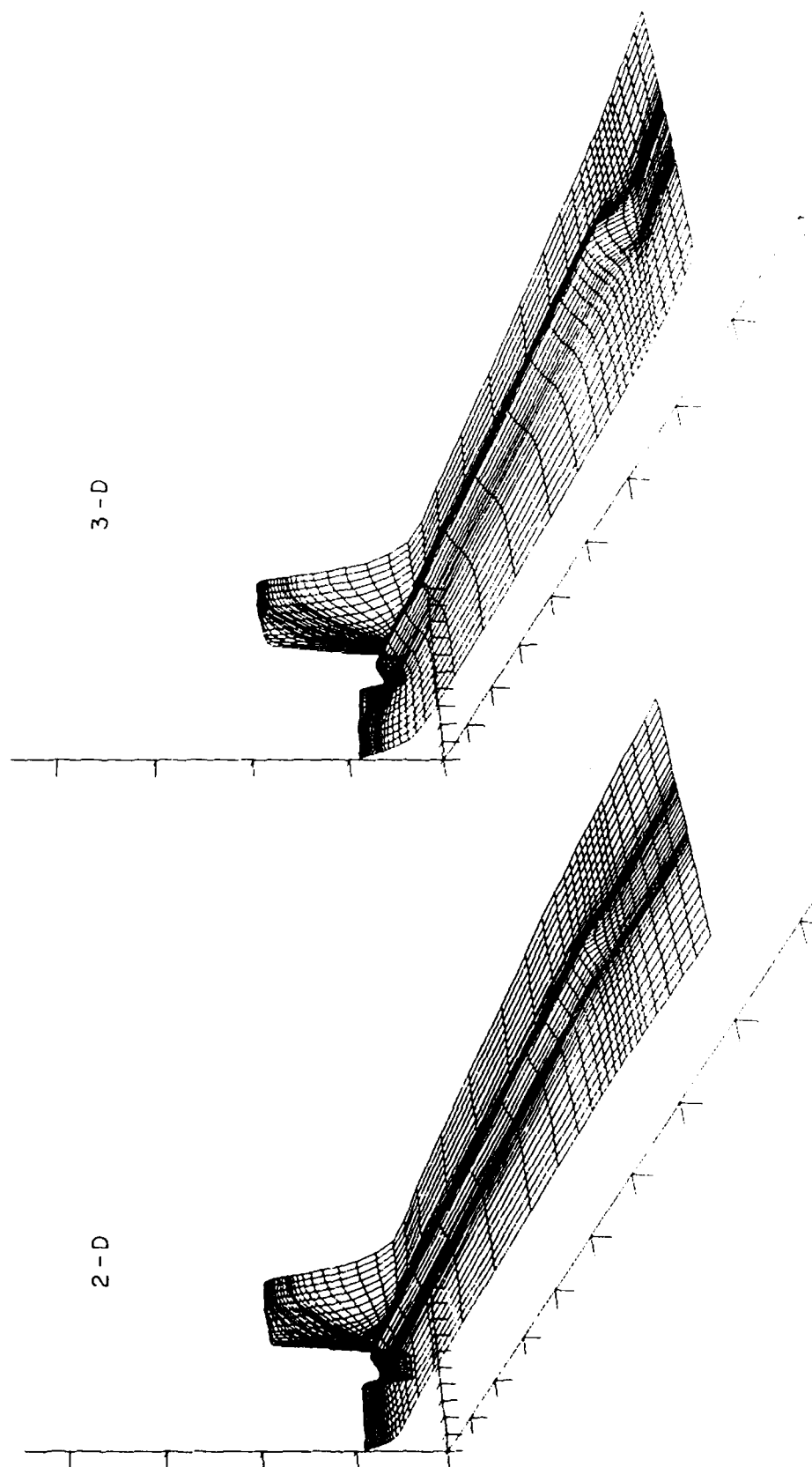


Figure 21. Comparison of 2-D and 3-D result for potential surface in the X-Z plane of the particle track 10 psec following the strike.

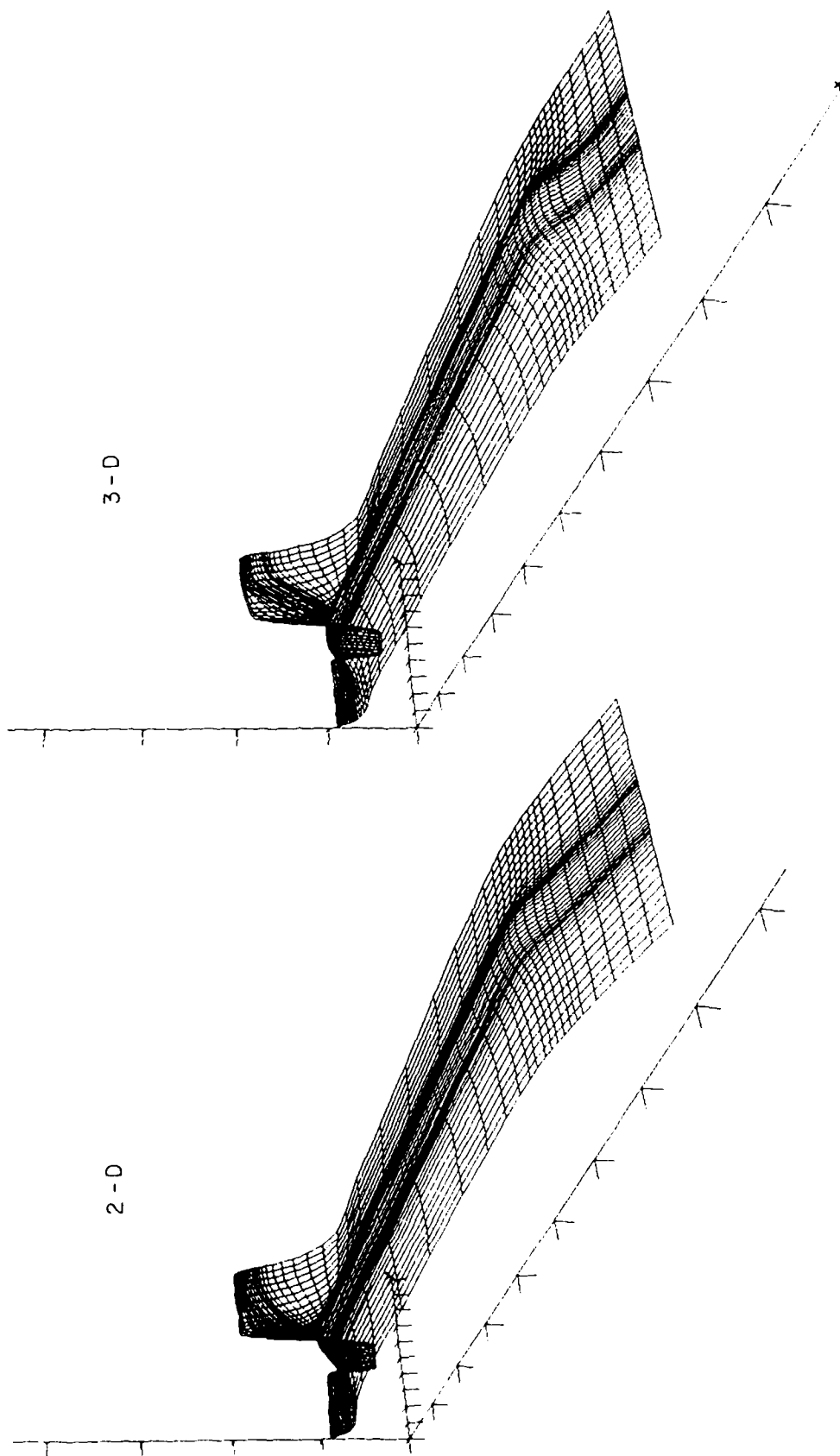


Figure 22. Same as Figure 21 except at $T = 40$ psec.

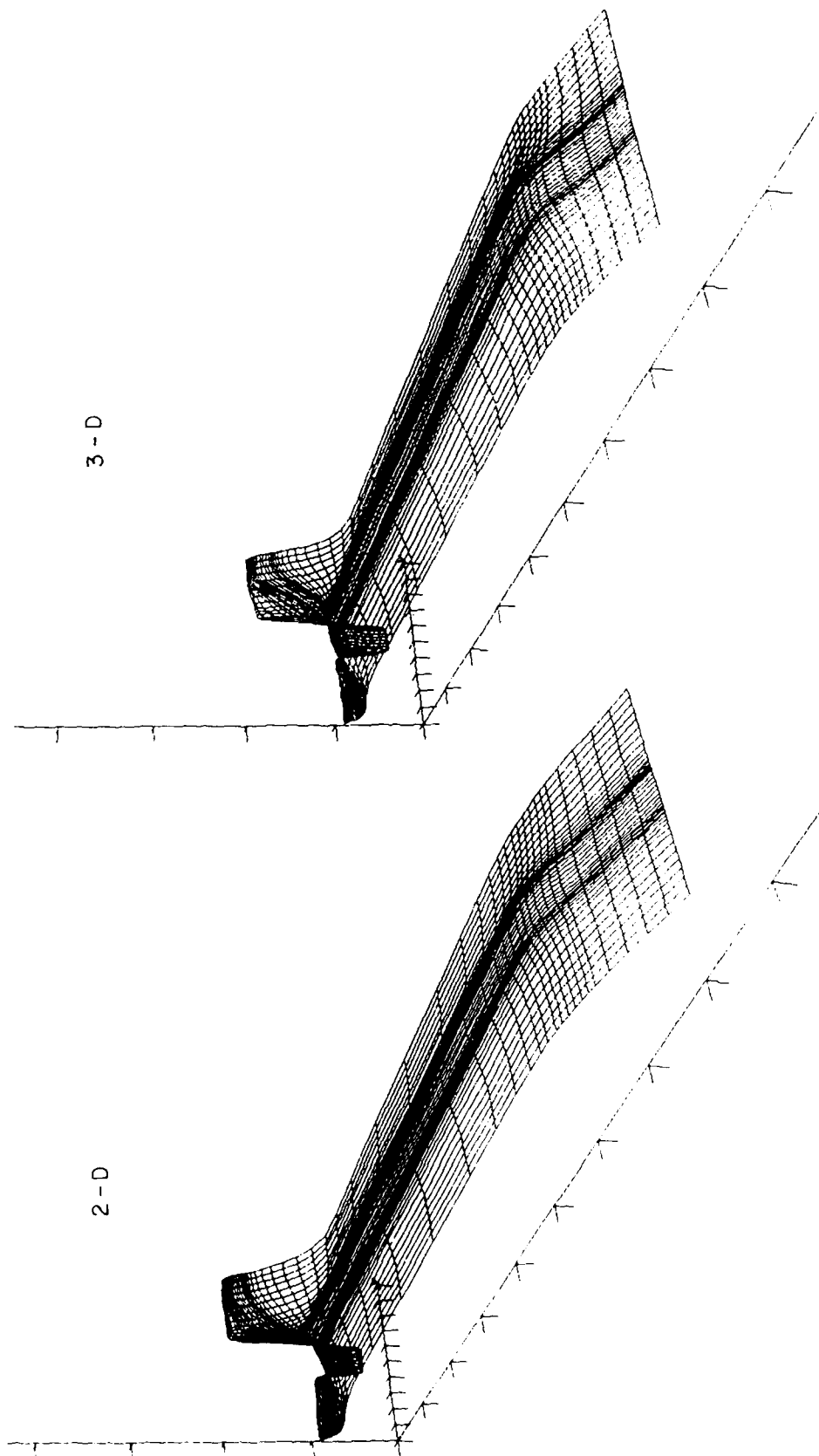


Figure 23. Same as Figure 21 except at $T = 100$ psec.

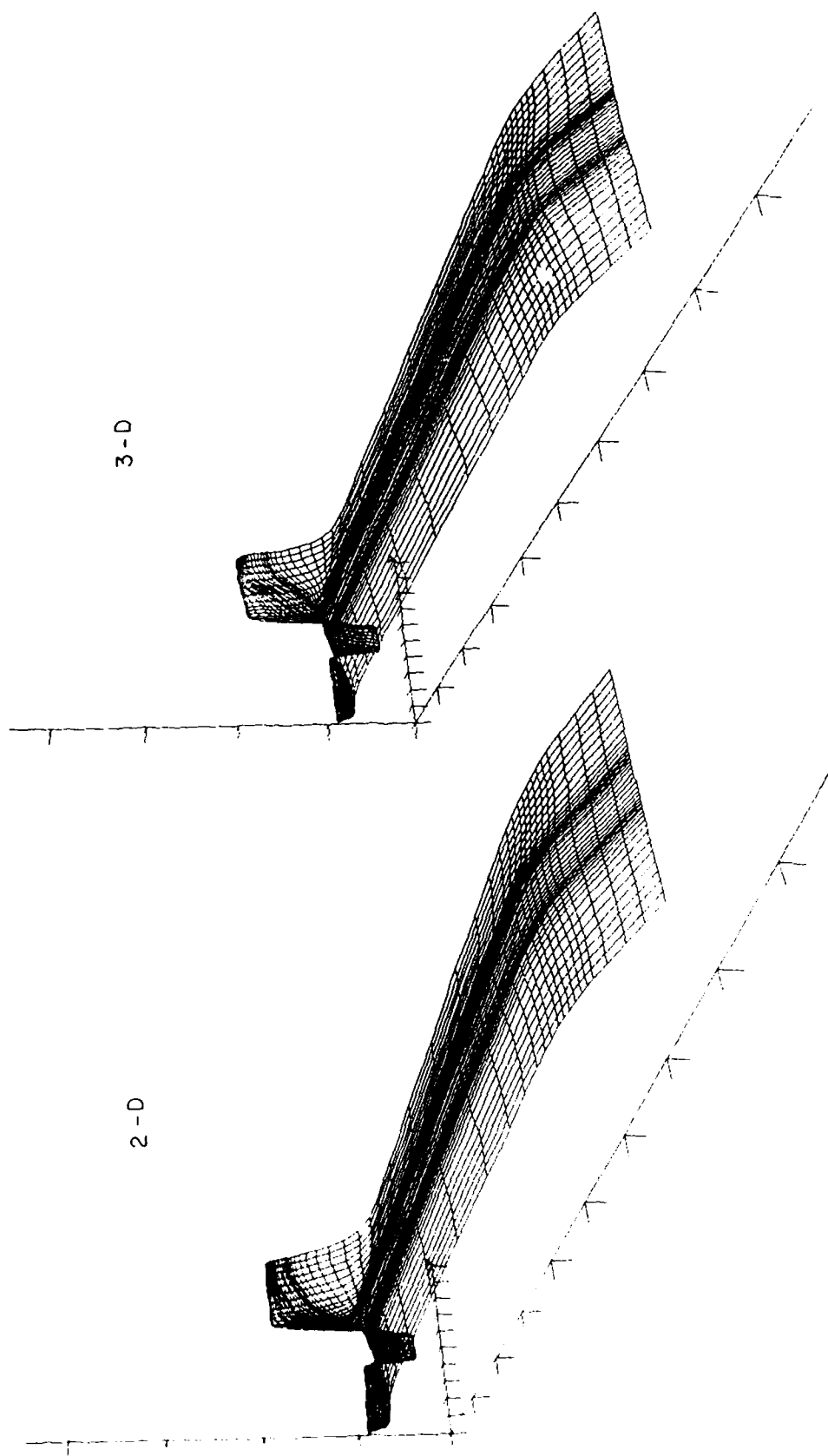


Figure 24. Same as Figure 21 except at $T = 200$ psec.

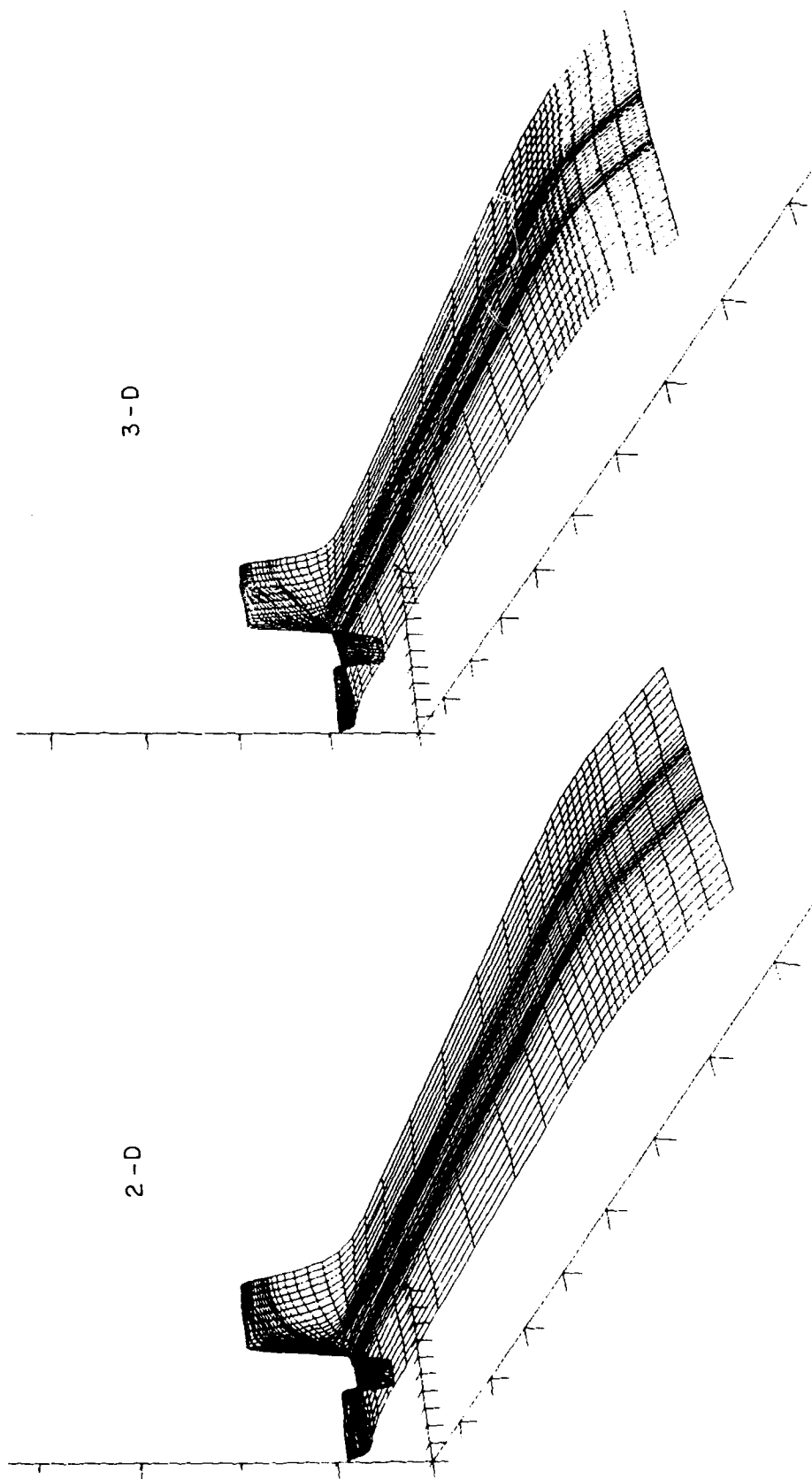


Figure 25. Same as Figure 21 except at $T = 400$ psec.

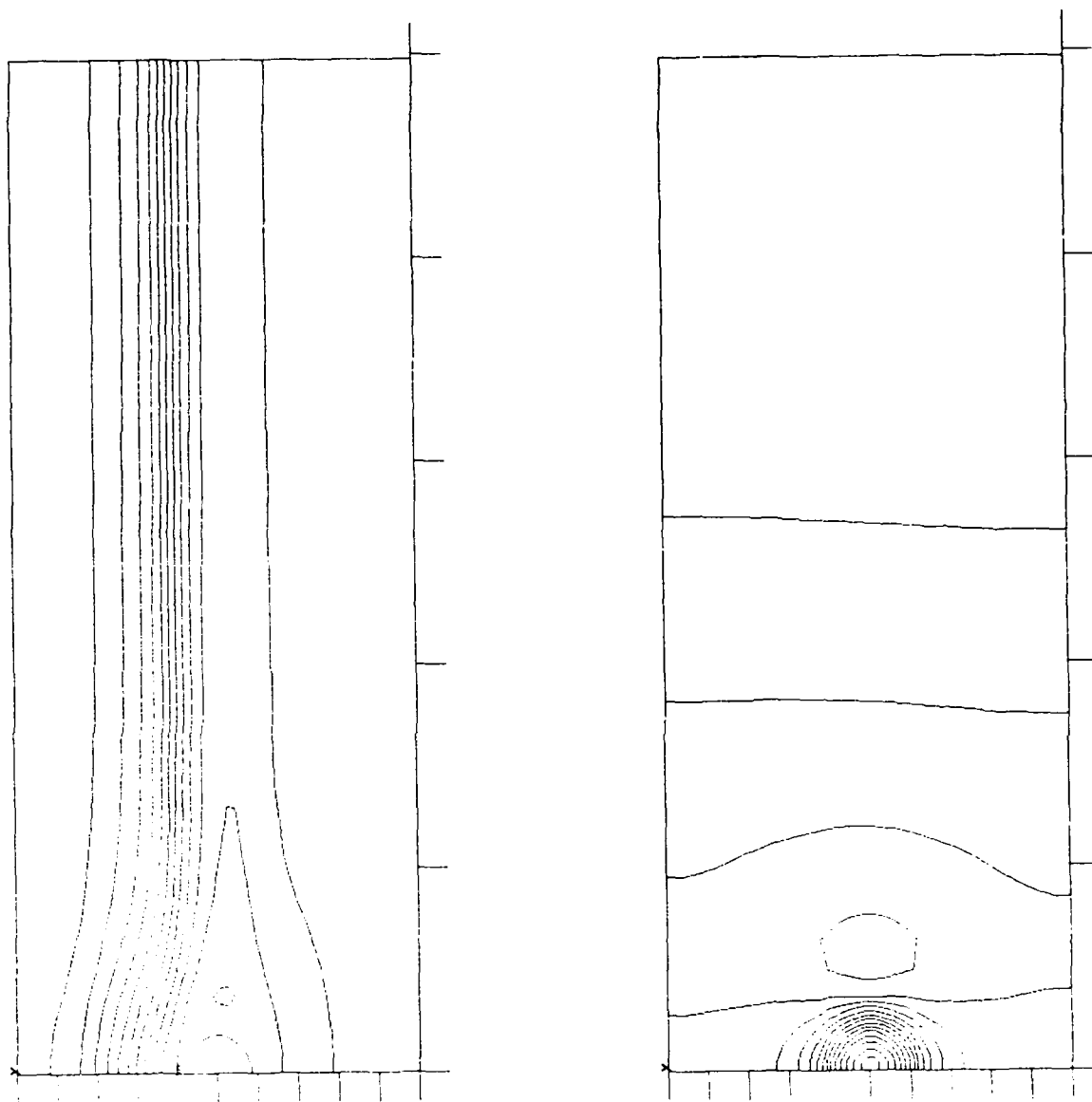


Figure 26. Potential contours in two Y-Z planes.
 Left, $0.5 \mu\text{m}$ from the contact surface, in the
 channel and right, $8.24 \mu\text{m}$ from the
 contact surface, in the substrate, at $t = 10 \text{ psec}$.

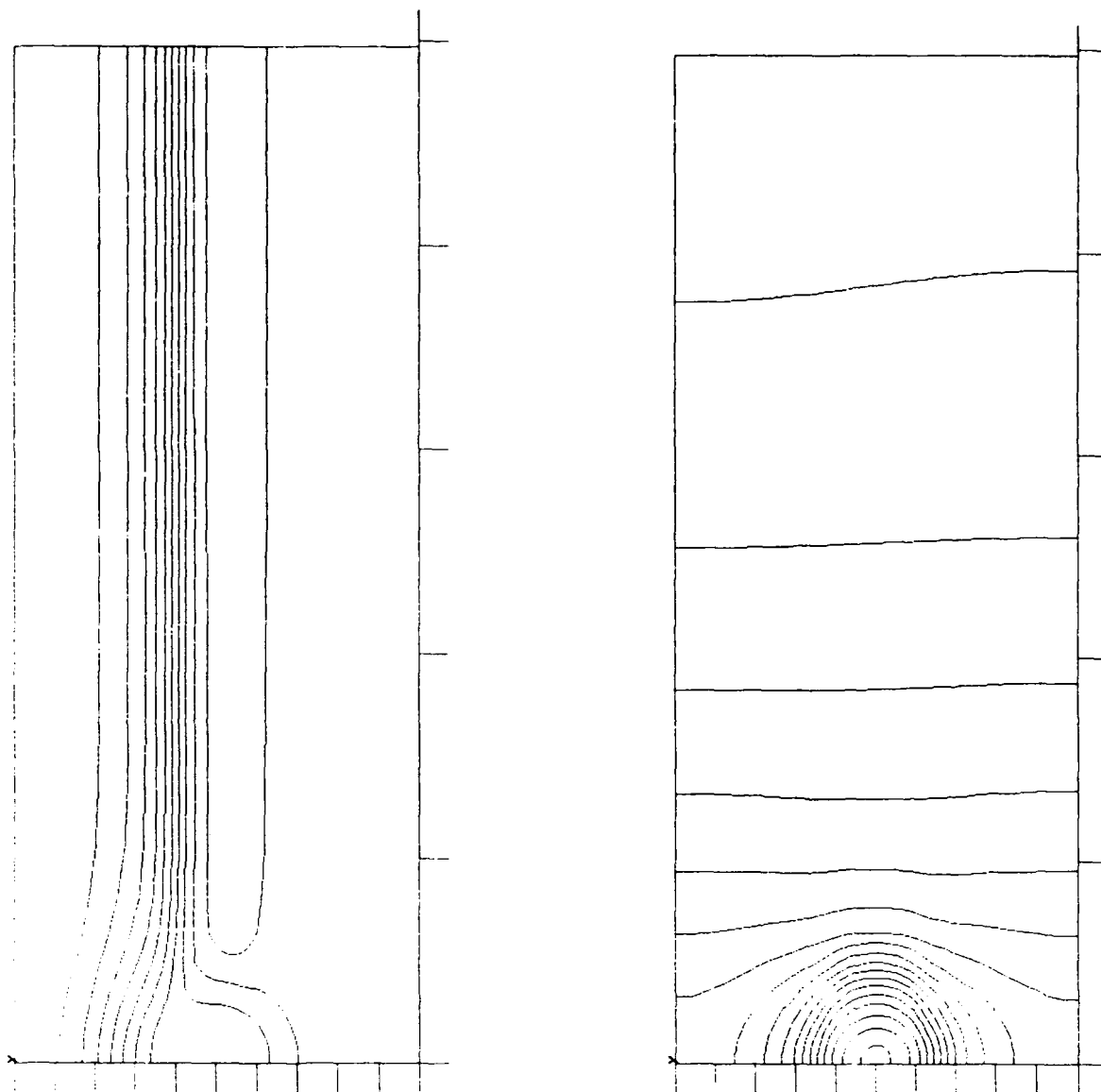


Figure 27. Potential contours in two Y-Z planes.
 Left, $0.5 \mu\text{m}$ from the contact surface, in the
 channel and right, $8.24 \mu\text{m}$ from the
 contact surface, in the substrate, at $t = 40 \text{ psec}$.

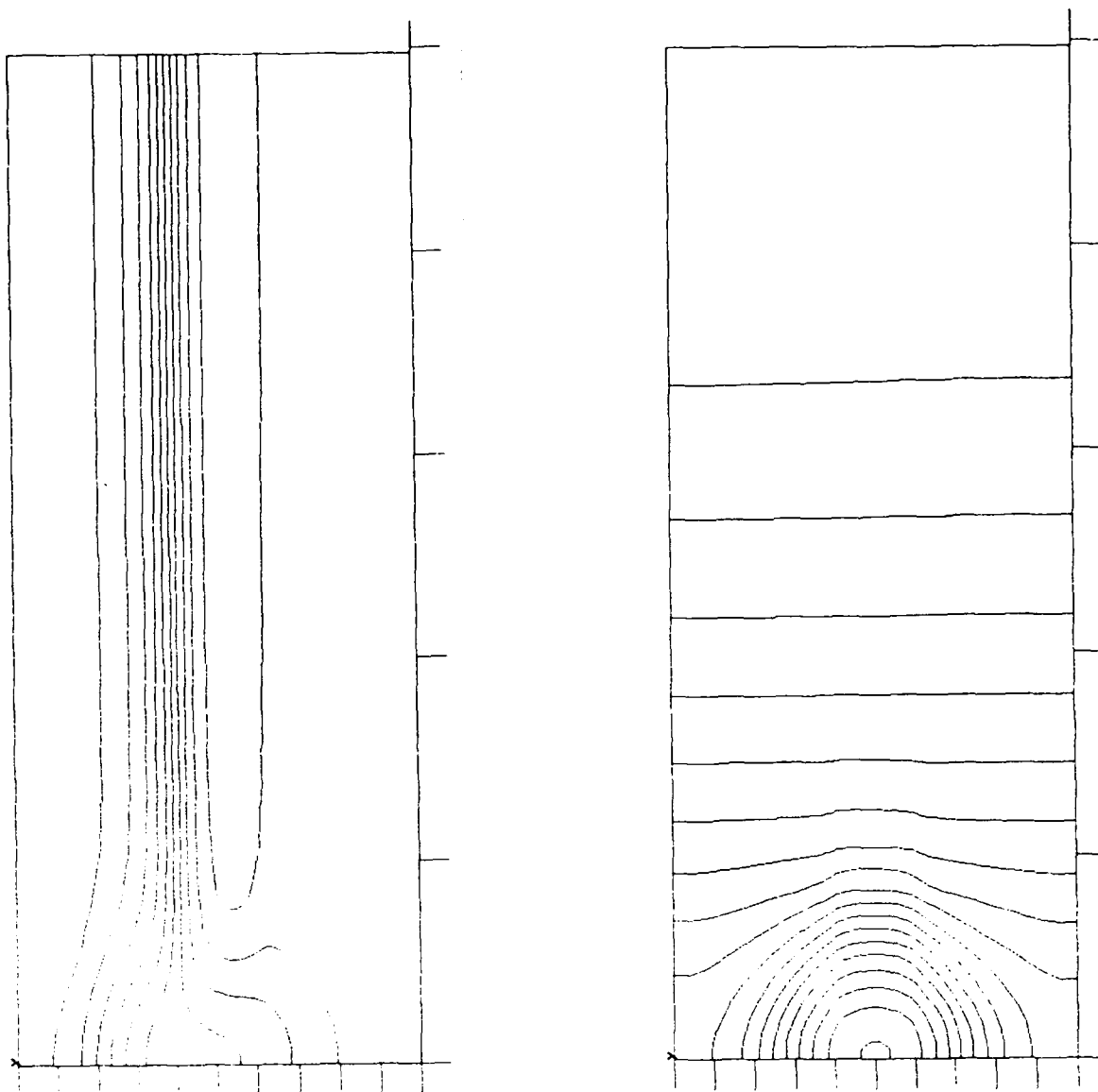


Figure 28. Potential contours in the Y-Z planes.
 Left, $0.5 \mu\text{m}$ from the contact surface, in the
 channel and right, $8.24 \mu\text{m}$ from the
 contact surface, in the substrate, at $t = 100 \text{ psec}$.

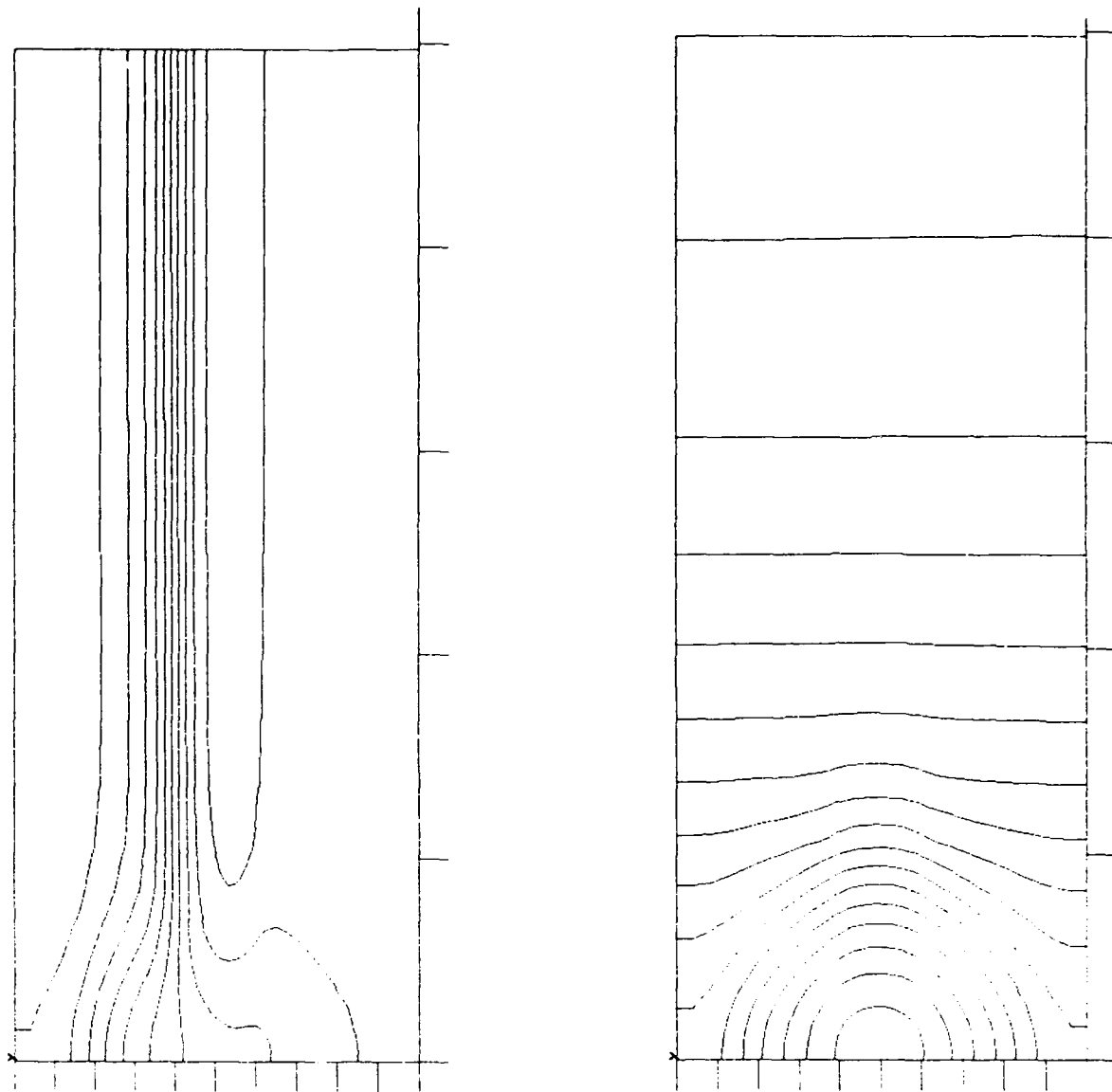


Figure 29. Potential contours in the Y-Z planes.
Left, $0.5 \mu\text{m}$ from the contact surface, in the
channel and right, $8.24 \mu\text{m}$ from the
contact surface, in the substrate, at $t = 200 \text{ psec.}$

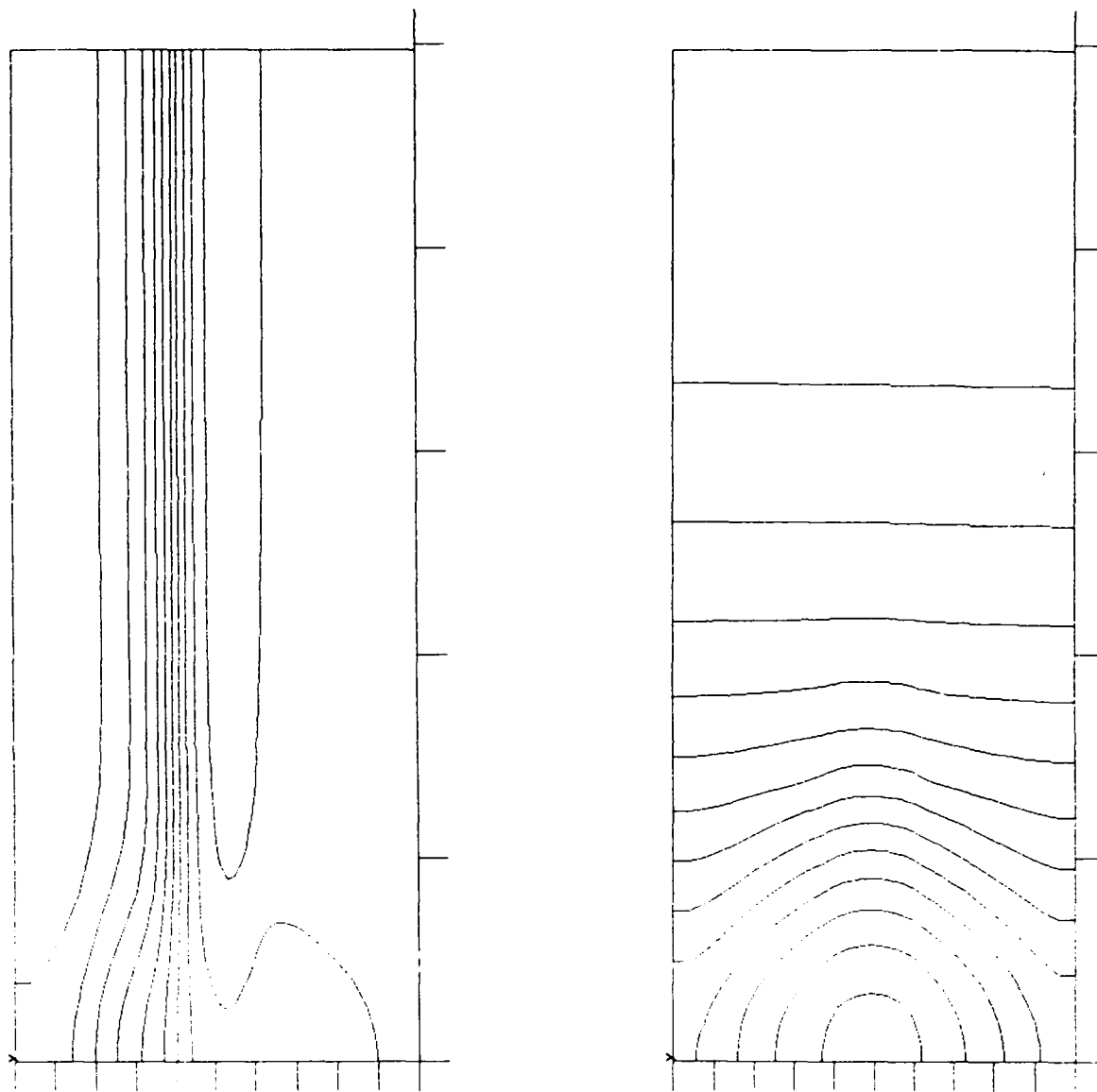


Figure 30. Potential contours in the Y-Z planes.
Left, $0.5 \mu\text{m}$ from the contact surface, in the
channel and right, $8.24 \mu\text{m}$ from the
contact surface, in the substrate, at $t = 400 \text{ psec}$.

Distribution list for "Simulation of the Response of a Gallium Arsenide JFET to Single Particle Radiation in Two and Three Dimensions".

	No. Copies
Naval Research Laboratory Attn: Dr. Edward Peterson, Code 4611 4555 Overlook Avenue, S.W. Washington, DC 20375	1
Mr. LeRoy Dombkowski UAA/J9 DCASMA 96 Murphy Road Hartford, CT 06114-2173	1
Director Naval Research Laboratory Attn: Code 2627 Washington, DC 20375	6
Defense Technology Information Center Bldg. 5, Cameron Station Alexandria, VA 22314	12

END

DATE

FILMED

8-88

DTIC